CellPress
Partner Journal

Molecular Plant
Research article

Phosphate-dependent regulation of vacuolar trafficking of OsSPX-MFSs is critical for maintaining intracellular phosphate homeostasis in rice

Runze Guo[1,2,3,5], Qi Zhang[1,3,4,5], Kun Qian[1,3,5], Yinghui Ying[1], Wenying Liao[1,2], Lening Gan[1,2], Chuanzao Mao[1], Yong Wang[3], James Whelan[1,3] and Huixia Shou[1,2,3,*]

[1]State Key Laboratory of Plant Physiology and Biochemistry, College of Life Sciences, Zhejiang University, Hangzhou, Zhejiang 310058, P.R. China

[2]Hainan Institute, Zhejiang University, Sanya 572025, China

[3]The Provincial International Science and Technology Cooperation Base on Engineering Biology, International Campus of Zhejiang University, Haining, Zhejiang 314400, China

[4]Zhijiang lab, Hangzhou 310012, China

[5]These authors contributed equally to this article.

***Correspondence: Huixia Shou (huixia@zju.edu.cn)**

https://doi.org/10.1016/j.molp.2023.07.004

ABSTRACT

Vacuolar storage of inorganic phosphate (Pi) is essential for Pi homeostasis in plants. The SPX-MFS family proteins have been demonstrated to be vacuolar Pi transporters in many plant species. Transcriptional regulation of the predominant transporter among rice SPX-MFSs, OsSPX-MFS3, was only moderately suppressed by Pi starvation. Thus, post-transcriptional mechanisms were hypothesized to regulate the activity of OsSPX-MFS3. In this study, we found that the tonoplast localization of OsSPX-MFSs is inhibited under Pi-depleted conditions, resulting in their retention in the pre-vacuolar compartments (PVCs). A yeast two-hybrid screen identified that two SNARE proteins, OsSYP21 and OsSYP22, interact with the MFS domain of OsSPX-MFS3. Further genetic and cytological analyses indicate that OsSYP21 and OsSYP22 facilitate trafficking of OsSPX-MFS3 from PVCs to the tonoplast. Although a homozygous frameshift mutation in *OsSYP22* appeared to be lethal, tonoplast localization of OsSPX-MFS3 was significantly inhibited in transgenic plants expressing a negative-dominant form of OsSYP22 (*OsSYP22-ND*), resulting in reduced vacuolar Pi concentrations in *OsSYP22-ND* plants. Under Pi-depleted conditions, the interaction between OsSYP22 and OsSPX-MFS3 was disrupted, and this process depended on the presence of the SPX domain. Deleting the SPX domains of OsSPX-MFSs resulted in their tonoplast localization under both Pi-depleted and Pi-replete conditions. Complementation of the *osspx-mfs1/2/3* triple mutants with the MFS domain or the SPX domain of OsSPX-MFS3 confirmed that the MFS and SPX domains are responsive to Pi transport activity and Pi-dependent regulation, respectively. These data indicated that the SPX domains of OsSPX-MFSs sense cellular Pi (InsP) levels and, under Pi-depleted conditions, inhibit the interaction between OsSPX-MFSs and OsSYP21/22 and subsequent trafficking of OsSPX-MFSs from PVCs to the tonoplast.

Guo R., Zhang Q., Qian K., Ying Y., Liao W., Gan L., Mao C., Wang Y., Whelan J., and Shou H. (2023). Phosphate-dependent regulation of vacuolar trafficking of OsSPX-MFSs is critical for maintaining intracellular phosphate homeostasis in rice. Mol. Plant. **16**, 1304–1320.

INTRODUCTION

Phosphorus (P) is essential for all life and a key element in photosynthesis, respiration, and the biosynthesis of nucleic acids and membranes in plants (Lambers, 2021). P is acquired as inorganic phosphate (Pi) and is one of the most abundant macronutrients in plant tissues. Pi forms insoluble complexes or precipitates with organic matter or mineral cations, which are

Published by the Molecular Plant Shanghai Editorial Office in association with Cell Press, an imprint of Elsevier Inc., on behalf of CSPB and CEMPS, CAS.

easily immobilized in the soil. Consequently, nearly 70% of global cultivated land suffers from Pi deficiency that compromises plant growth and crop yields. Plants have evolved sophisticated strategies to cope with low Pi availability, involving transcriptional, post-transcriptional, metabolic, and morphological adaptations. These adaptations coordinate Pi sensing, signaling, uptake, allocation, and recycling oriented toward maintaining cellular Pi homeostasis, improving Pi acquisition, and protecting plants from the stress caused by low Pi availability (Smith and Barker, 2002; Chiou and Lin, 2011; Gutierrez-Alanis et al., 2018).

The vacuole serves as the primary intracellular compartment for storage and remobilization of Pi and thus plays a pivotal role in plant Pi homeostasis (Bucher and Fabianska, 2016). Under adequate Pi supply, up to 95% of intracellular Pi is stored in the vacuole (Bucher and Fabianska, 2016). When plants suffer from phosphate deficiency, the Pi stored in vacuoles is released into the cytoplasm to meet P requirements for cellular activity and growth. Recent studies have identified SPX-MFS vacuolar Pi transporters (also named VPTs or PHT5), with both SYG1/PHO81/XPR1 (SPX) and major facilitator superfamily (MFS) domains, that sequester Pi in the vacuolar lumen of *Arabidopsis* and rice. In *Arabidopsis*, VPT1 plays a predominant role, and VPT3 is particularly important when VPT1 is absent (Liu et al., 2015, 2016; Luan et al., 2019). The *vpt1* mutant exhibited a lower vacuolar/cytoplasmic Pi ratio than wild-type controls, but *VPT1* overexpression lines showed reduced growth and accumulated more Pi in their vacuoles relative to the cytosol. A *vpt1 vpt3* double mutant showed altered systemic phosphate allocation and was impaired in reproductive development. Similar to their homologs in *Arabidopsis*, the three rice (*Oryza sativa*) SPX-MFSs (OsSPX-MFS1 through 3) also localize in the tonoplast and function as Pi influx transporters (Wang et al., 2015). Although the role of SPX-MFSs in buffering cellular Pi has been characterized, the regulatory mechanism by which plants sense cyt-Pi to regulate SPX-MFS function remains unknown.

SPX domains are found in eukaryotic phosphate transporters, signaling proteins, and inorganic polyphosphate polymerases and are involved in phosphate homeostasis (Secco et al., 2012a, 2012b; Puga et al., 2014). SPX domains provide a basic binding surface for inositol pyrophosphate (PP-InsP), whose concentrations change in response to Pi availability (Lonetti et al., 2011; Wild et al., 2016; Zhu et al., 2019a). Substitutions of critical binding-surface residues in the SPX domain impair InsP binding *in vitro*, inorganic polyphosphate synthesis in yeast, and Pi transport in *Arabidopsis* (Wild et al., 2016). In plants, there are four subfamilies of SPX domain-containing proteins: SPX-EXS (named after *Saccharomyces cerevisiae* Erd1, mammalian Xpr1, and *S. cerevisiae* Syg1), SPX-MFS, SPX-RING, and SPXs (small proteins with only the SPX domain; Secco et al., 2012b). SPX proteins can interact with a multitude of proteins, such as PHR1 (phosphate starvation response 1) and PHL1 (PHR1-like 1) in *Arabidopsis* and OsPHR2 in rice, to transduce the Pi signal and regulate cellular Pi homeostasis (Lv et al., 2014; Puga et al., 2014; Wang et al., 2014; Wild et al., 2016; Dong et al., 2019; Ried et al., 2021). Increased PP-InsP levels were recently shown to promote the interaction of SPX domains with PHR to block the Pi starvation response under Pi-sufficient conditions (Ried et al., 2021; Zhou et al., 2021; Guan et al., 2022). By contrast, mutation of genes for synthesis of InsPs resulted in constitutive expression of phosphate-starvation-induced genes (Zhu et al., 2019a).

Soluble N-ethylmaleimide-sensitive factor attachment protein receptors (SNAREs), which are highly conserved in eukaryotic cells, control vesicle budding and fusion as well as the trafficking of membrane proteins to their final destinations (Jahn and Scheller, 2006; Colombo et al., 2014). According to the conserved amino acids of their SNARE motifs, SNARE proteins can be classified into Qa-, Qb-, Qc-, SNAP25-like, and R-SNAREs. A functional SNARE complex consists of a four-helical bundle assembled by four SNARE motifs, including three Q-SNAREs (localized to the target membrane) and one R-SNARE (localized to the vesicle membrane; Wickner, 2010). SYP2 (syntaxin of plants 2) proteins, a subfamily of Qa-SNAREs, are thought to participate in the fusion of vesicles with pre-vacuolar compartments (PVCs) or vacuoles. The *Arabidopsis* genome encodes three *SYP2* genes, *SYP21*, *SYP22*, and *SYP23*, and a proposed pseudogene, *SYP24* (Sanderfoot et al., 2000; Uemura et al., 2004). SYP21/22 localize to the tonoplasts and PVCs, whereas SYP23 localizes to the cytosol (Foresti et al., 2006; Uemura et al., 2010; Zhu et al., 2019b). Expression of *SYP23* suppressed the abnormal *syp22* phenotype (Shirakawa et al., 2010). Thus, SYP2 proteins appear to function redundantly in vacuolar trafficking and plant development. Furthermore, they all can form a complex with the Qb-SNARE VTI11, the Qc-SNARE SYP5, and the R-SNARE VAMP727 (Sanderfoot et al., 2001; Yano et al., 2003; Ebine et al., 2008).

To determine the mechanism by which SPX-MFSs are regulated in response to cellular Pi levels, we screened a cDNA library in yeast for OsSPX-MFS3 interacting proteins. We identified two SNARE proteins, OsSYP21 and OsSYP22. These proteins are localized on the PVCs and tonoplasts and directly interact with OsSPX-MFS3 to facilitate vacuolar trafficking of OsSPX-MFS3. Under Pi-depleted conditions, the SPX domain of OsSPX-MSF3 interacts with the MFS domain and blocks the binding region recognized by OsSYP22. This inhibits PVC-to-vacuole trafficking of OsSPX-MFS3 and thus reduces cytosol-to-vacuole Pi partitioning, facilitating adaptation to Pi-depleted conditions.

RESULTS

Tonoplast localization of OsSPX-MFSs is inhibited under Pi-depleted conditions

SPX-MFS family genes encode plant vacuolar Pi influx transporter proteins that contribute to cytosol-to-vacuole Pi partitioning (Liu et al., 2015, 2016; Wang et al., 2015). The major contributor in rice, *OsSPX-MFS3*, showed a weak transcriptional response to changes in cellular Pi levels (Wang et al., 2012; Secco et al., 2013; Guo et al., 2022). We hypothesized that rice *SPX-MFSs* might be regulated in a post-translational manner. We investigated the subcellular localization of GFP-tagged OsSPX-MFSs (whose cDNA was driven by the CaMV 35S promoter) under Pi-replete and Pi-depleted conditions. When GFP-OsSPX-MFSs were transiently expressed in rice protoplasts, two localization patterns were observed: a tonoplast pattern and a non-tonoplast pattern in which GFP-OsSPX-MFSs appeared to be localized in

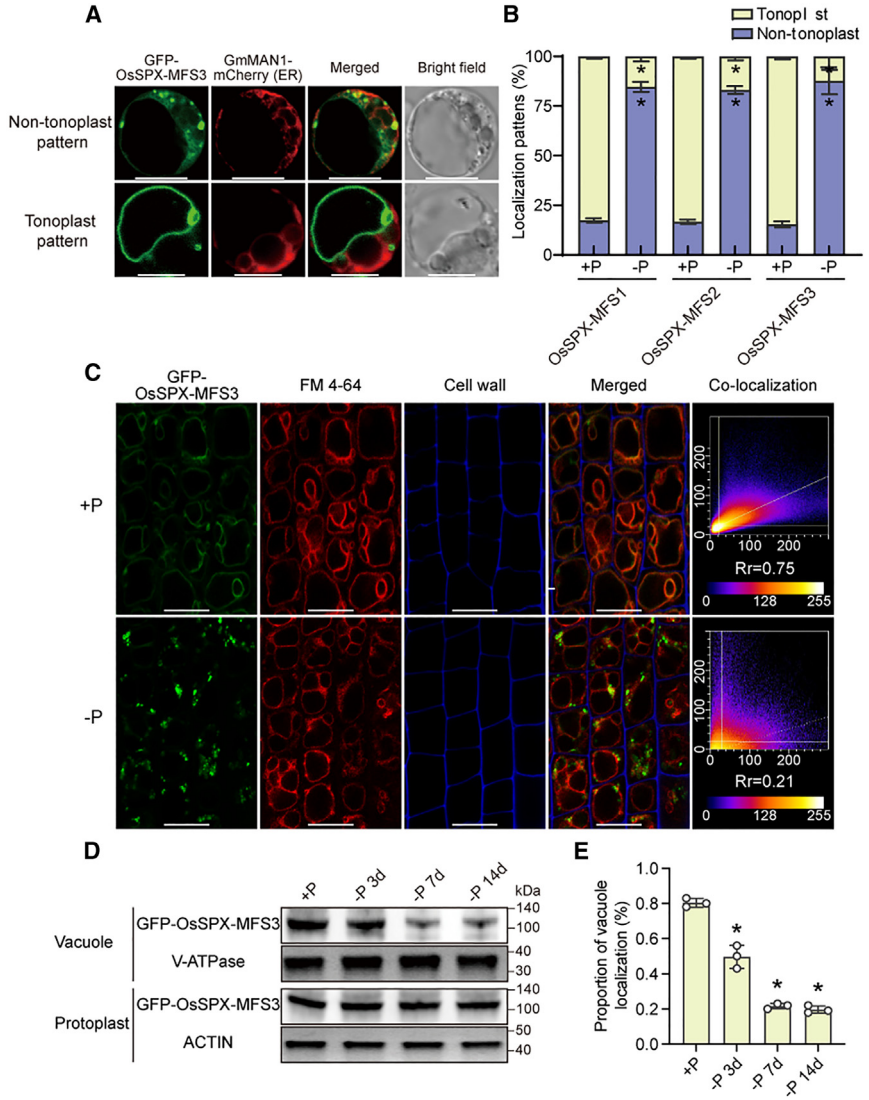

Figure 1. Tonoplast localization of OsSPX-MFSs is inhibited under Pi-depleted conditions.

(A) Subcellular localization of OsSPX-MFSs. The tonoplast and non-tonoplast localization patterns of GFP-OsSPX-MFSs are shown. Scale bars, 20 μm.

(B) Quantification of GFP-OsSPX-MFS localization patterns under Pi-replete or Pi-depleted conditions. More than 150 protoplasts were counted.

(C) Confocal fluorescence imaging of root cells from *GFP-OsSPX-MFS3* overexpression plants grown under Pi-replete or Pi-depleted conditions. Tonoplasts were stained for 3 h with the endocytotic tracer FM4-64 (5 μM). Scale bars, 20 μm. Co-localization analyses were performed using Coloc2 in ImageJ software. Rr represents the Pearson correlation coefficient.

(D and E) Effect of Pi supply on distributions of GFP-OsSPX-MFS3 in protoplasts and vacuoles. Two-week-old *GFP-OsSPX-MFS3* overexpression plants were transferred to Pi-depleted conditions for the number of days indicated. Protoplasts and tonoplasts were isolated, immunoblotted using GFP antibodies **(D)**, and quantified **(E)**. Rice β-actin and V-ATPase were detected as references for protoplast and vacuolar proteins, respectively. * indicates a significant difference relative to +P ($p \leq 0.05$, two-tailed Student's t test). Values are mean ± SD; n = 3 biological replicates.

endomembrane compartments and small vesicles (Figure 1A). Quantification of the localization patterns under Pi-replete and Pi-depleted conditions showed that the tonoplast localization of OsSPX-MFSs was inhibited under Pi-depleted conditions. Approximately 80% of the protoplasts transformed with each of the GFP-tagged rice SPX-MFS proteins displayed the tonoplast pattern under Pi-replete conditions. By contrast, under Pi-depleted conditions, only about 20% of protoplasts displayed this pattern (Figure 1B).

We next examined the effect of low cellular Pi level on subcellular localization of OsSPX-MFS3 *in planta*. We investigated the subcellular localization of GFP-tagged OsSPX-MFS3 in the root maturation zone adjacent to the meristem zone in transgenic plants overexpressing *GFP-OsSPX-MFS3* (driven by the CaMV35S promotor). Both fast-growing cells with multiple small vacuoles and mature cells with single large vacuoles are present in this zone. The endocytic pathway dye FM4-64 was used to stain tonoplasts. Long-term uptake led to a high accumulation of FM4-64 at the tonoplast 3 h after application. GFP-OsSPX-MFS3 mainly displayed tonoplast localization and was present in a few small, dot-like structures, putatively PVCs, in roots under Pi-replete conditions (Figure 1C). The Pearson coefficient of GFP-OsSPX-MFS3 and FM4-64 was as high as 0.75. By contrast, GFP-OsSPX-MFS3 was detected mainly on the small, dot-like structures under Pi-depleted conditions, and there was a low Pearson coefficient between GFP-OsSPX-MFS3 and FM4-64 (Figure 1C). There was no difference in total fluorescence intensity between Pi-replete and Pi-depleted conditions (Supplemental Table 1). Protoplasts and vacuoles were then isolated from *GFP-OsSPX-MFS3* overexpression plants to detect the effects of Pi concentration on OsSPX-MFS3 distribution by immunoblotting. The amount of GFP-OsSPX-MFS3 protein in whole protoplast cells did not change significantly after exposure to Pi-depleted conditions (Figure 1D). However, the amount of GFP-OsSPX-MFS3 protein in the tonoplasts was reduced to 35% and 30% after exposure to low-Pi conditions for 1 and 2 weeks, respectively (Figures 1D and 1E).

On the basis of these observations, we hypothesized that low cellular Pi inhibits trafficking of GFP-OsSPX-MFS3 to the tonoplast. Trafficking of tonoplast proteins in the secretory pathway can occur via Golgi-dependent or Golgi-independent pathways (Rojas-Pierce, 2013; Di Sansebastiano et al., 2017). The Golgi-dependent pathway involves a series of organelles including the endoplasmic reticulum (ER), Golgi apparatus, trans-Golgi network (TGN), PVCs, and vacuole, whereas the Golgi-independent

pathway delivers proteins directly from the ER to the PVCs. To determine which step of OsSPX-MFS trafficking was blocked under Pi-depleted conditions, we investigated the pathway transporting OsSPX-MFSs from the ER to the vacuole. After treatment with the fungal toxin brefeldin A (BFA), an inhibitor of ER-to-Golgi trafficking (Robinson et al., 2008), GFP-OsSPX-MFS3 was retained in the ER, indicating that OsSPX-MFS3 is trafficked via the Golgi-dependent pathway (Figures 2A and 2B). A set of organelle markers for the ER (AtWAK2), Golgi (GmMAN1), TGN (VHA-A1), and PVC (AtARA7) were co-expressed to determine the localization of OsSPX-MFS3 under Pi-depleted conditions. GFP-OsSPX-MFS3 localized mainly to the PVCs with a minor portion in other endomembrane systems such as the ER, Golgi, and TGN (Figure 2C). A time course of FM4-64 staining was performed to confirm the possible co-localization of these punctate GFP-SPX-MFS3s in rice root cells. FM4-64 reached the early endosome (TGN) by 5 min and the late endosome (MVB/PVC) by 15–30 min. Under Pi-depleted conditions, GFP-SPX-MFS3 was not co-localized with FM4-64 after 5 min of staining (Figure 2D) but was mainly co-localized with FM4-64 after 15 min of staining (Figure 2D). Treatment with wortmannin (which induces PVC enlargement) enlarged the GFP signal of GFP-SPX-MFS3 (Figure 2E, arrowhead), confirming that GFP-SPX-MFS3 was in the PVCs.

These results demonstrate that the tonoplast protein OsSPX-MFS3 is trafficked via the Golgi-dependent pathway. Under Pi-depleted conditions, trafficking of OsSPX-MFS3 between the PVCs and the vacuole was disrupted, and OsSPX-MFS3 was retained mainly in the PVCs, thus limiting the capacity for vacuolar Pi sequestration in response to cellular Pi concentration.

OsSYP21 and OsSYP22 interact with the MFS domain of OsSPX-MFSs

To elucidate the mechanism by which tonoplast localization of OsSPX-MFSs was inhibited under Pi-depleted conditions, we screened a rice seedling cDNA library for proteins that interacted with OsSPX-MFS3 (the major vacuolar Pi transporter) using a split-ubiquitin membrane-based yeast two-hybrid (Y2H) system. We identified multiple independent cDNAs encoding a putative SNARE protein, LOC_Os01g15110, designated OsSYP22. Conserved domain analysis showed that OsSYP22 contained putative SynN (cl29093) and t-SNARE (cl22856) domains and a C-terminal transmembrane (TM) helix. OsSYP22 had one paralogous protein, OsSYP21 (LOC_Os02g47440), in the rice SYP2 subfamily (Supplemental Figure 1). *OsSYP22* and its paralog *OsSYP21* were relatively highly expressed in leaves, an expression pattern similar to that of *OsSPX-MFS3*, as revealed by qRT–PCR analysis (Supplemental Figure 2).

We used Cub-SPX-MFS3^{SPX}, Cub-SPX-MFS3$^{SPX\text{-}2TM}$, Cub-SPX-MFS3$^{SPX\text{-}6TM}$, and Cub-SPX-MFS3 as baits to verify the initial library screening (Figure 3A; Supplemental Table 2). Additional Y2H assays showed that truncated versions of OsSPX-MFS3 containing the SPX domain and the first two or six TM helices of the MFS domain, OsSPX-MFS3$^{SPX\text{-}6TM}$ and OsSPX-MFS3$^{SPX\text{-}2TM}$, could interact with OsSYP21 and OsSYP22 in yeast (Figure 3B). The SPX domain alone did not interact with OsSYP21 and OsSYP22 in yeast (Figure 3B). To further investigate which domain of OsSYP21/22 was involved in their interaction with OsSPX-MFS3, OsSYP21/22 were truncated into OsSYP21/22$^{SynN+t\text{-}SNARE}$ (missing the C-terminal TM helices), OsSYP21/22$^{t\text{-}SNARE}$ (missing the SynN domain and C-terminal TM helices) and OsSYP21/22^{SynN} (SynN domain only) as prey constructs (Figure 3A; Supplemental Table 2). The Y2H results showed that the N-terminal SynN domain of OsSYP21/22, but not the t-SNARE domain alone, could interact with OsSPX-MFS3 (Figure 3B). This result indicated that the N-terminal SynN domain of OsSYP21/22 contributed to the interaction between OsSYP21/22 and OsSPX-MFS3. This interaction was also observed between OsSPX-MFS1/2 and OsSYP21/22 (Supplemental Figure 3A). Notably, the *Arabidopsis* paralogs of OsSPY21/22, AtSYP21, AtSYP22, and AtSYP23, display high sequence identity and similarity to OsSPY21/22 (Supplemental Figure 1B). Y2H assays showed that the *Arabidopsis* AtSYP2 subfamily (AtSYP21–23) could also interact with AtVPTs (AtVPT1–3; Supplemental Figure 3A).

OsSYP21 and OsSYP22 localized on both the PVCs and the tonoplasts (Supplemental Figure 4A), consistent with the localization of their *Arabidopsis* orthologs (Foresti et al., 2006; Uemura et al., 2010). Co-expression of GFP fused to OsSYP21 or OsSYP22 with mCherry fused to OsSPX-MFS3 in rice protoplasts resulted in overlapping fluorescence signals, indicating that the proteins co-localized (Supplemental Figure 4B).

Bimolecular fluorescence complementation (BiFC) assays were performed to further confirm the interaction between OsSYP21/22 and OsSPX-MFSs. To ensure that nYFP and cYFP in the fusion proteins were in the same cellular compartment, we used redox-based topology analysis (ReTA), based on fusion of TM proteins with redox-sensitive GFP (roGFP2) and ratiometric imaging, to determine the TM topology of OsSPX-MFS3 and OsSYP21/22. Vacuolar intrinsic membrane proteins established the final topology of each protein across the membrane as soon as they entered the endomembrane system by co-translational translocation into the ER. The results showed that roGFP2-OsSYP21/22 displayed a low 405/488 nm florescence ratio (Figures 3C and 3D), consistent with previous reports that the N terminus of SNAREs is exposed to the cytosol. By contrast, fusion of roGFP to the C-terminus of OsSYP21/22 resulted in a high 405/488 nm fluorescence ratio, indicative of an oxidized roGFP tag localized to the luminal side of the membrane (Figures 3C and 3D). When roGFP was fused to the N- or C-terminus of OsSPX-MFS3, roGFP displayed a low 405/488 nm florescence ratio, confirming that the N and C termini of OsSPX-MFS3 and the N terminus of OsSYP21/22 were present in the same cellular compartment (Figures 3C and 3D). BiFC assays with nYFP-OsSPX-MFS3 and cYFP-OsSYP21/22 in tobacco leaves resulted in a YFP fluorescence signal, confirming that the proteins interacted. Negative controls that co-expressed YFP-OsSPX-MFS3/cYFP or nYFP/OsSYP21/22 did not produce a detectable fluorescence signal (Figure 3E). Similar interactions were observed between OsSYP21/22 and OsSPX-MFS1 or OsSPX-MFS2 (Supplemental Figure 3B). Co-immunoprecipitation (Co-IP) assays were performed in tobacco leaves by co-transforming GFP-OsSPX-MFS3, GFP-OsSPX-MFS3^{MFS} (lacking the N-terminal 222 amino acids corresponding to the SPX domain), or GFP-OsSPX-MFS3^{SPX} (lacking the C-terminal 476 amino acids corresponding to the MFS domain) with FLAG-OsSYP21/22. Both OsSYP21 and OsSYP22 interacted with OsSPX-MFS3 and GFP-OsSPX-MFS3^{MFS}, but not

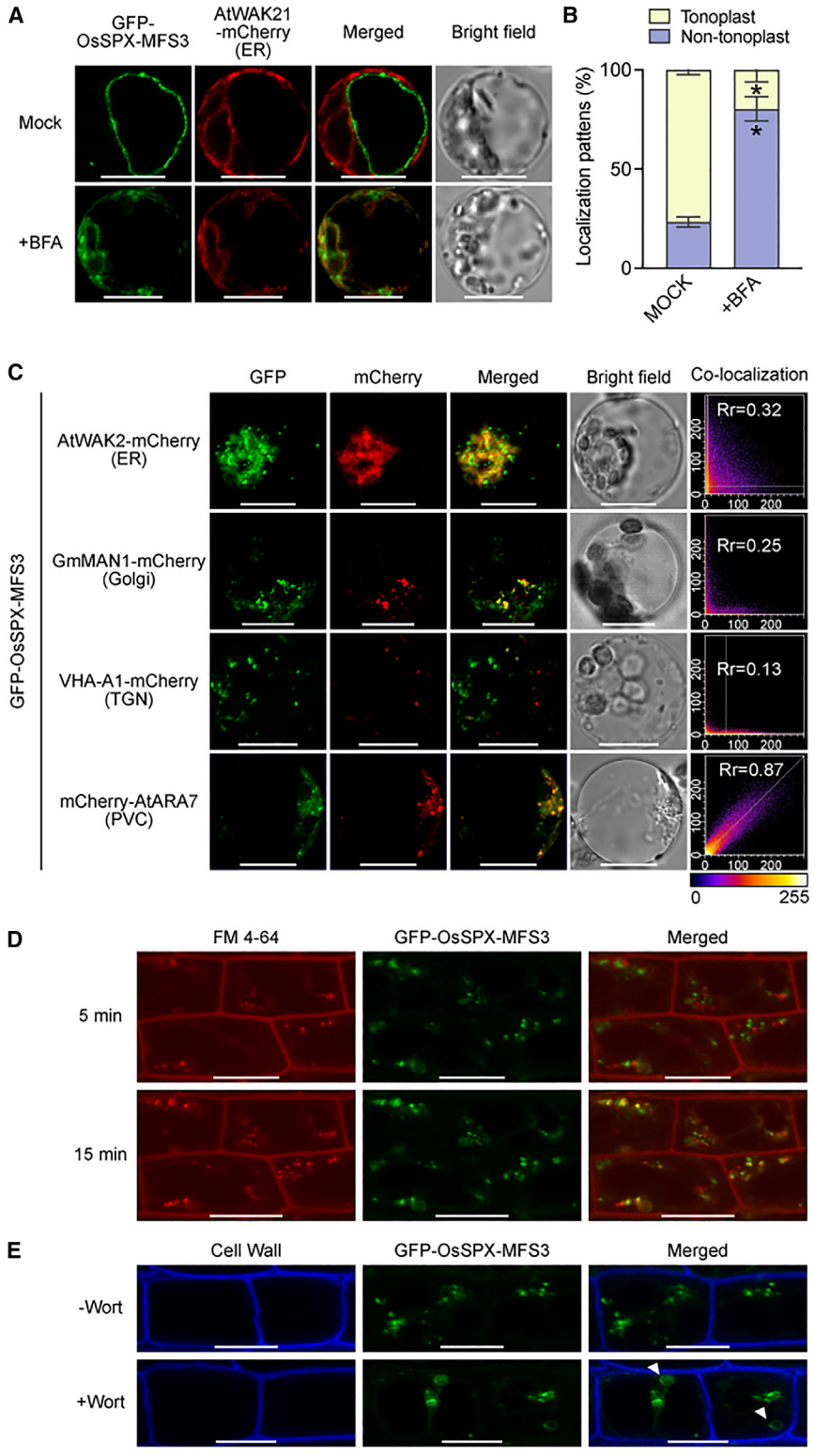

Figure 2. OsSPX-MFS3 is predominantly retained in the PVCs under Pi-depleted conditions.

(A) Brefeldin A (BFA) blocks trafficking of GFP-OsSPX-MFS3. GFP-OsSPX-MFS3 was retained in the ER after incubation with 50 μM BFA for 8 h. Scale bar, 20 μm.

(B) Quantification of GFP-OsSPX-MFS localization patterns with and without BFA treatment.

(C) Localization of GFP-OsSPX-MFS3 in protoplasts prepared from rice plants grown under Pi-depleted conditions. mCherry-tagged AtWAK2, GmMAN1, VHA-A1, and AtARA7 were used as ER, Golgi, TGN, and PVC markers of endomembrane systems. Scale bar, 20 μm.

(D) Time course of FM4-64 staining of root cells from *GFP-OsSPX-MFS3* transgenic rice grown under Pi-depleted conditions. Scale bars, 20 μm.

(E) Subcellular distribution of GFP-OsSPX-MFS3 in root cells treated with 33 μM wortmannin for 2 h. Scale bars, 20 μm. Wortmannin-induced compartments in treated cells are indicated by arrowheads.

with GFP-OsSPX-MFS3^{SPX} (Figure 3F). Thus, the interaction requires the MFS domain of OsSPX-MFS3 (Figure 3F).

Taken together, these results show that the SYP2 subfamily proteins can interact with SPX-MFS family proteins in rice and very likely also in *Arabidopsis*.

OsSYP22 is required for trafficking of OsSPX-MFS3

Newly synthesized membrane proteins are initially targeted to the ER and then delivered to the Golgi apparatus for modification and further sorting within the endomembrane system. SNARE proteins regulate vesicle budding and membrane fusion (Jahn et al., 2003; Sudhof and Rothman, 2009). We therefore hypothesized that the interaction of OsSYP21/22 with OsSPX-MFS3 facilitates targeting of OsSPX-MFS3 to the tonoplast, as shown above. To test this hypothesis, we attempted to generate *ossyp21* and *ossyp22* knockout mutants using a CRISPR/Cas9 system. Two independent mutants, *ossyp21-1* and *ossyp21-2*, identified by sequencing analysis, contained a 1-bp insertion and a 1-bp deletion, respectively, in the fourth exon of *OsSYP21* (Supplemental Figures 5A and 5B). However, we were unable to obtain a homozygous frameshift mutant of *OsSYP22*. In the T0 generation, we identified four heterozygous mutant lines that contained one frameshifted allele and one non-frameshifted allele (Supplemental Figure 5B). However, none of the heterozygous plants produced a homozygous frameshift mutant in the T1 generation, indicating that a homozygous frameshift mutation of *OsSYP22* might be lethal. Transient expression of mCherry-OsSPX-MFS3 in protoplasts from *ossyp21* or *OsSYP22*$^{+/-}$ plants resulted in a localization pattern (~80% in tonoplasts) similar to that of wild-type (NIP) protoplasts under Pi-replete conditions (Figure 4A; Supplemental Figure 5C), indicating that

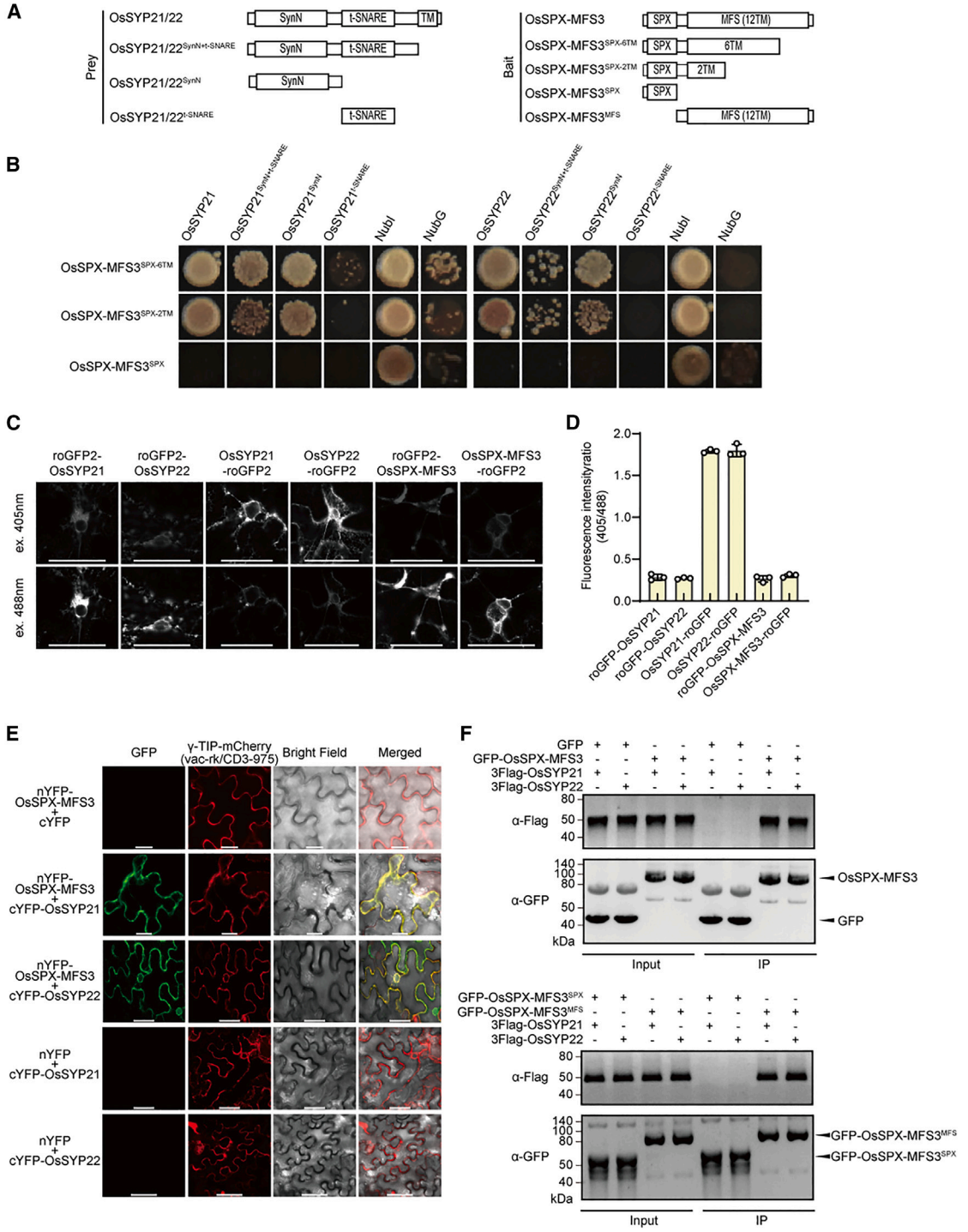

Figure 3. OsSPX-MFS3 interacts with OsSYP21 and OsSYP22.

(A) Schematic diagram of full-length and truncated versions of OsSYP-MFS3 and OsSYP21/22.

(B) Split-ubiquitin yeast two-hybrid analysis of OsSYP21/22 and OsSPX-MFS3. Full-length and truncated versions of OsSPX-MFS3 and OsSYP21/22 were used as bait and prey proteins, respectively. Yeast transformants were cultured on selection medium QDO, 3-AT (-Leu-Trp-His-Ade, 10 mM 3-AT). Cub, C-terminal ubiquitin; NubI and NubG, wild-type and mutated N-terminal fragment of ubiquitin.

(C) Redox-based topology analysis (ReTA) of OsSYP21/22 and OsSPX-MFS3. Fluorescence images of roGFP2-OsSYP21/22, OsSYP21/22-roGFP2, roGFP2-OsSPX-MFS3, and OsSPX-MFS3-roGFP excited by 405 and 488 nm laser. Tobacco leaf epidermal cells were used for transient expression of the corresponding roGFP2-fused proteins. Incubation with 50 μM brefeldin A (BFA) for 8 h was used to block the transfer of tonoplast proteins through the secretory pathway to the Golgi before serial optical sections were obtained. Scale bars, 50 μm.

(legend continued on next page)

the tonoplast localization of OsSPX-MFS3 was unaffected in the *ossyp21* and *OsSYP22*$^{+/-}$ mutants.

We next generated transgenic rice that expressed a negative-dominant form of *OsSYP22*, *OsSYP22-ND*. *OsSYP22-ND* was produced by overexpressing a truncated version of *OsSYP22* lacking the region encoding the C-terminal TM helices (Supplemental Figure 6). The truncated OsSYP22 competed with endogenous OsSYP22 for interaction with other SNARE complex components. When mCherry-OsSPX-MFS3 was transiently expressed in protoplasts of *OsSYP22-ND* lines, the tonoplast localization of mCherry-OsSPX-MFS3 was inhibited, resulting in a punctate pattern (Figures 4A and 4B). Thus, the negative-dominant form of OsSYP22 led to retention of OsSPX-MFS3 in PVCs, whereas *ossyp21* mutants and *OsSYP22*$^{+/-}$ lines showed no changes in OsSPX-MFS3 localization, indicating that the SYP2 subfamily proteins involved in the SNARE complex are essential for trafficking of OsSPX-MFS3 to the tonoplast.

OsSYP21 and OsSYP22 play a positive role in cytosol-to-vacuole Pi partitioning

Because OsSPX-MFS3 functions as the major plant vacuolar Pi influx transporter (Wang et al., 2015; Guo et al., 2022) and OsSYP22 directly regulates the trafficking of OsSPX-MFS3 between PVCs and vacuoles, we hypothesized that OsSYP22 plays a positive role in cytosol-to-vacuolar Pi partitioning. To test this hypothesis, we analyzed the phenotypes of *OsSYP22-ND* and *OsSYP22* overexpression lines (Supplemental Figure 6). Forty-day-old *OsSYP22-ND* and *OsSYP22* overexpression plants had significant growth defects compared with NIP under Pi-replete conditions. The *OsSYP22-ND* plants were smaller than the *OsSYP22* overexpression lines (Figure 4C). Consistent with our hypothesis, the vacuolar Pi concentration of *OsSYP22-ND* plants was about 75% of that in NIP plants. The vacuolar Pi concentration of *OsSYP22* overexpression lines was about 130% of that in the NIP plants (Figure 4D). Pi concentrations in the shoots and roots of the *OsSYP22-ND* and *OsSYP22* overexpression lines were not significantly different from those of NIP (Supplemental Figures 7A and 7B). By contrast, 40-day-old *ossyp21* mutant plants did not differ from NIP plants in biomass, vacuolar Pi concentration, or leaf and root Pi content (Supplemental Figures 7C–7G), whereas the *OsSYP21* overexpression plants had a phenotype similar to that of *OsSYP22* overexpression plants. The vacuolar Pi concentration of *OsSYP21* overexpression lines was higher than that of NIP, and their biomass was lower (Supplemental Figures 7C–7G). Shoot and root Pi concentrations of the *OsSYP21* overexpression lines did not differ significantly from those of NIP, suggesting that OsSYP21 and OsSYP22 have similar functions in rice Pi homeostasis.

To clarify the effect of OsSYP21/22 and OsSPX-MFSs on vacuolar Pi sequestration, *OsSYP21* and *OsSYP22* were individually overexpressed in the *osspx-mfs1/2/3* triple mutant (Guo et al., 2022). Two independent representative overexpression lines of *OsSYP21* and *OsSYP22* were chosen for further analysis (Figure 4E). Overexpression of *OsSYP21* or *OsSYP22* did not increase vacuolar Pi concentration in the *osspx-mfs1/2/3* triple mutant background (Figure 4F), indicating that the role of OsSYP21/22 on vacuolar Pi sequestration is dependent on functional rice SPX-MFSs.

The SPX domain inhibits interaction of the MFS domain with OsSYP22 under Pi-depleted conditions

The SPX domain has been shown to bind PP-InsPs with high affinity to sense cellular Pi availability (Wild et al., 2016; Jung et al., 2018; Ried et al., 2021). We next examined the role of the SPX domain in OsSPX-MFS protein trafficking by examining the localization of GFP-tagged OsSPX-MFSs^{MFS} in rice protoplasts. The results showed that OsSPX-MFSs^{MFS} and full-length proteins had similar localization patterns under Pi-replete conditions and displayed tonoplast localization in most protoplasts (Supplemental Figure 8A). However, OsSPX-MFS3^{MFS} displayed a tonoplast localization pattern in most protoplasts under Pi-depleted conditions as well (Supplemental Figure 8A). We also tested the localization of OsSPX-MFS3^{MFS} in GFP-OsSPX-MFS3^{MFS} overexpression plants grown under Pi-depleted conditions. Consistent with the results of transient expression in protoplasts, fluorescence imaging showed that GFP-OsSPX-MFS3^{MFS} and GFP-OsSPX-MFS3 had similar localization patterns under Pi-replete conditions (Figure 5A). In contrast to GFP-OsSPX-MFS3, which changed location when grown under Pi-depleted conditions, GFP-OsSPX-MFS3^{MFS} displayed a similar tonoplast localization pattern under both Pi-replete and Pi-depleted conditions (Figure 5A). An immunoblotting assay with GFP-OsSPX-MFS3^{MFS} protein contents from protoplasts and vacuoles showed that the amount of GFP-OsSPX-MFS3^{MFS} in the vacuole did not change when plants were transferred to Pi-depleted medium (Figures 5B and 5C). Thus, the SPX domain functions as a negative regulator of OsSPX-MFS3 trafficking under Pi-depleted conditions.

OsSYP22 physically interacts with OsSPX-MFS3 and regulates its trafficking from the PVCs to the tonoplast under Pi-replete conditions, but OsSPX-MFS3 is retained in the PVCs under Pi-depleted conditions. To determine whether the retention of OsSPX-MFS3 under Pi limitation occurs at or upstream of its interaction with OsSYP22, we examined whether *OsSYP22* responded to changes in cellular Pi levels. Two-week-old *pro35S-GFP-OsSYP22-1* seedlings were transferred from Pi-replete to Pi-depleted conditions. Samples were taken before and during the 2 weeks after

(D) Fluorescence ratios (405 nm/488 nm) for N- and C-terminal fusions of OsSPX-MFS3 and OsSYP21/22. roGFP displayed a low fluorescence ratio in the cytosol and a high fluorescence ratio in the ER lumen.

(E) BiFC analysis of the interaction between OsSPX-MFS3 and OsSYP21/22 in tobacco leaves. The N- and C-terminal fragments of YFP were fused to the N terminus of OsSPX-MFS3 (nYFP-OsSPX-MFS3) and the N terminus of OsSYP21/22 (cYFP-OsSYP21/22), respectively. Combinations of nYFP or cYFP with the corresponding OsSPX-MFS3 and OsSYP21/22 fusion constructs were used as negative controls. The location of the tonoplast is indicated by the expression of the tonoplast marker vac-rk (CD3-975). Scale bars, 50 μm.

(F) Co-immunoprecipitation (Co-IP) assay of OsSPX-MFS3 with OsSYP21/22 *in planta*. Plasmids containing *pro35S-GFP-OsSPX-MFS3* (or *OsSPX-MFS3*^{MFS} or *OsSPX-MFS3*^{SPX}) were co-transformed into tobacco leaves with *pro35S-3FLAG-OsSYP21/22*. Anti-GFP magnetic beads were used for IP, followed by immunoblotting with anti-FLAG and anti-GFP antibodies.

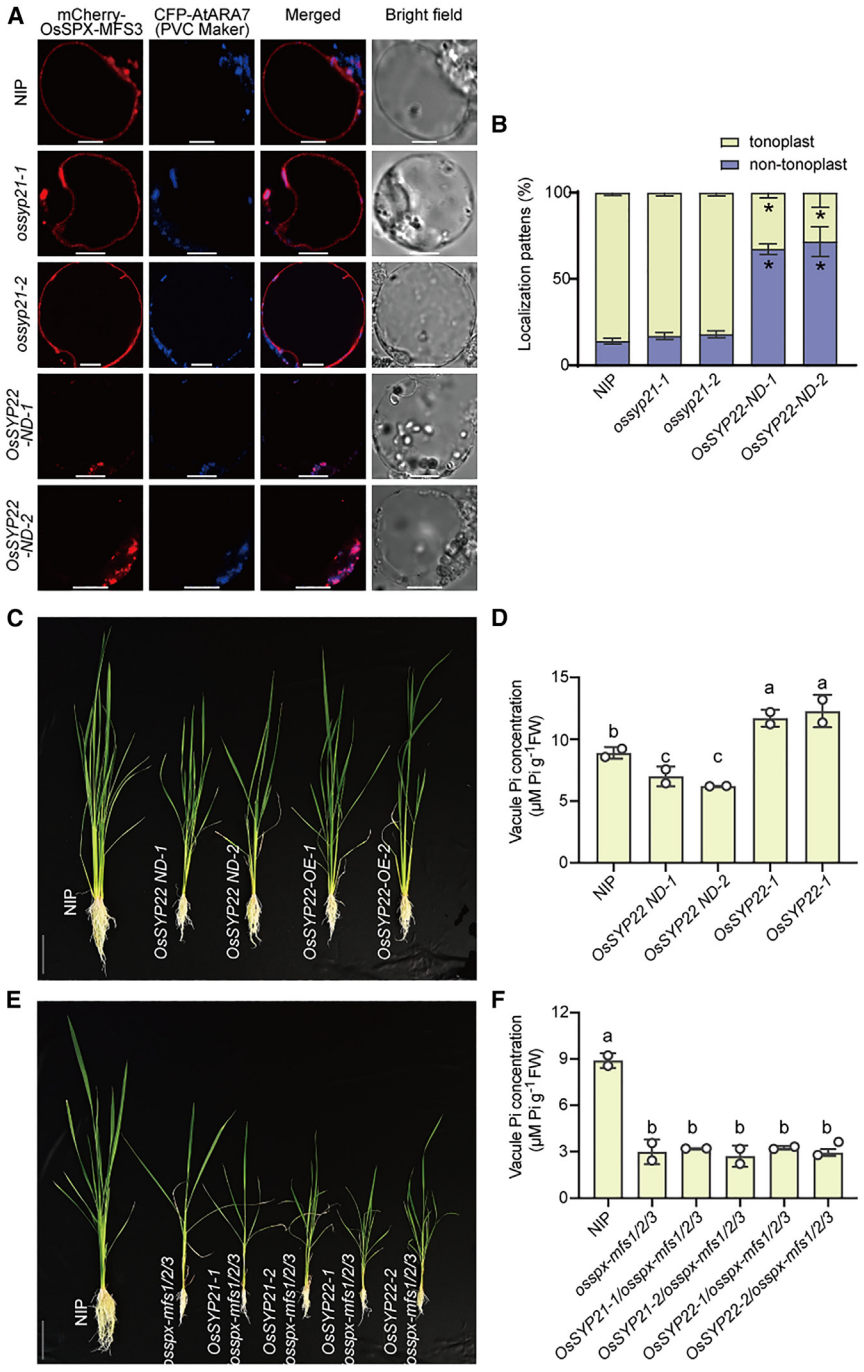

Figure 4. OsSYP22 is required for the trafficking of OsSPX-MFS3.

(A and B) Localization **(A)** and quantification **(B)** of mCherry-OsSPX-MFS3 in protoplasts isolated from NIP, *ossyp21* mutants, and *OsSYP22-ND* plants.

(C and D) Phenotypic performance **(C)** and root vacuolar Pi (Vac-Pi) concentrations **(D)** of 40-day-old NIP (wild-type), *OsSYP22-ND*, and *OsSYP22-OE* lines grown in Pi-replete conditions. Scale bars, 10 cm.

(E and F) Phenotypic performance **(E)** and root Vac-Pi concentrations **(F)** of 40-day-old NIP (wild-type), *osspx-mfs1/2/3*, and overexpression lines of *OsSYP21* (*OsSYP21*-OE) and *OsSYP22* (*OsSYP22*-OE) in the *osspx-mfs1/2/3* background grown in Pi-replete conditions. Scale bars, 10 cm. Different letters above each bar indicate statistically significant differences ($p < 0.05$, Tukey's honestly significant difference [HSD] test). Error bars indicate ±SD; n = 3 biological replicates. FW, fresh weight.

Pi-depletion treatment for qRT–PCR and immunoblotting assays. The results showed that both OsSYP22 mRNA and protein levels were unchanged under Pi starvation (Supplemental Figures 9A and 9B). Subcellular localization analysis showed that there was no difference in OsSYP22 localization between Pi-replete and Pi-depleted conditions (Supplemental Figure 9C).

BiFC assays were performed to examine the interaction between OsSPX-MFS3 and OsSYP22 under Pi-depleted conditions. YFP fluorescence signals were detected in about 30% of protoplasts when nYFP-OsSPX-MFS3 and cYFP-OsSYP22 were expressed in protoplasts isolated from NIP cultured under Pi-replete conditions (the top panel on the left in Figure 5D; Supplemental Figure 8B). Thus, OsSPX-MFS3 and OsSYP22 interact in rice protoplasts, similar to observations in tobacco leaves. However, when these BiFC partners were co-expressed in protoplasts isolated from NIP cultured under Pi-depleted conditions, only a few (about 2%) protoplasts had a detectable YFP fluorescence signal (the top panel on the right in Figure 5D; Supplemental Figure 8B), suggesting that low cellular Pi level prevented OsSPX-MFS3 from interacting with OsSYP22. Note that OsSPX-MFS3^{MFS} was not retained in the PVCs but was successfully targeted to tonoplasts under Pi-depleted conditions. We further examined the interaction of nYFP-OsSPX-MFS3^{MFS} and cYFP-OsSYP22 under Pi-depleted conditions. A BiFC assays showed that these proteins interacted in protoplasts under Pi-depleted conditions (the 2nd panel on the right in Figure 5D; Supplemental Figure 8B). When mCherry-OsSPX-MFS3^{SPX} was co-expressed with nYFP-OsSPX-MFS3^{MFS} and cYFP-OsSYP22 in protoplasts under Pi-depleted conditions, there was no YFP signal in protoplasts with a detectable mCherry signal (the 4th panel on the right in Figure 5D; Supplemental Figure 8B). This result indicates that the interaction of the MFS domain of OsSPX-MFS3 with SYP22 is inhibited by the SPX domain under Pi-depleted conditions. Co-IP assays were performed using GFP-tagged OsSPX-MFS3, OsSPX-MFS3^{MFS}, and OsSPX-MFS3^{SPX} and 3FLAG-tagged OsSYP21 or OsSYP22. The results showed that the interaction between the MFS domain of OsSXP-MFS3 and OsSYP22 gradually weakened as the duration of Pi deficiency increased. A Co-IP assay could barely detect their interaction after exposure to Pi deficiency for 7 and 14 days (Figure 5E).

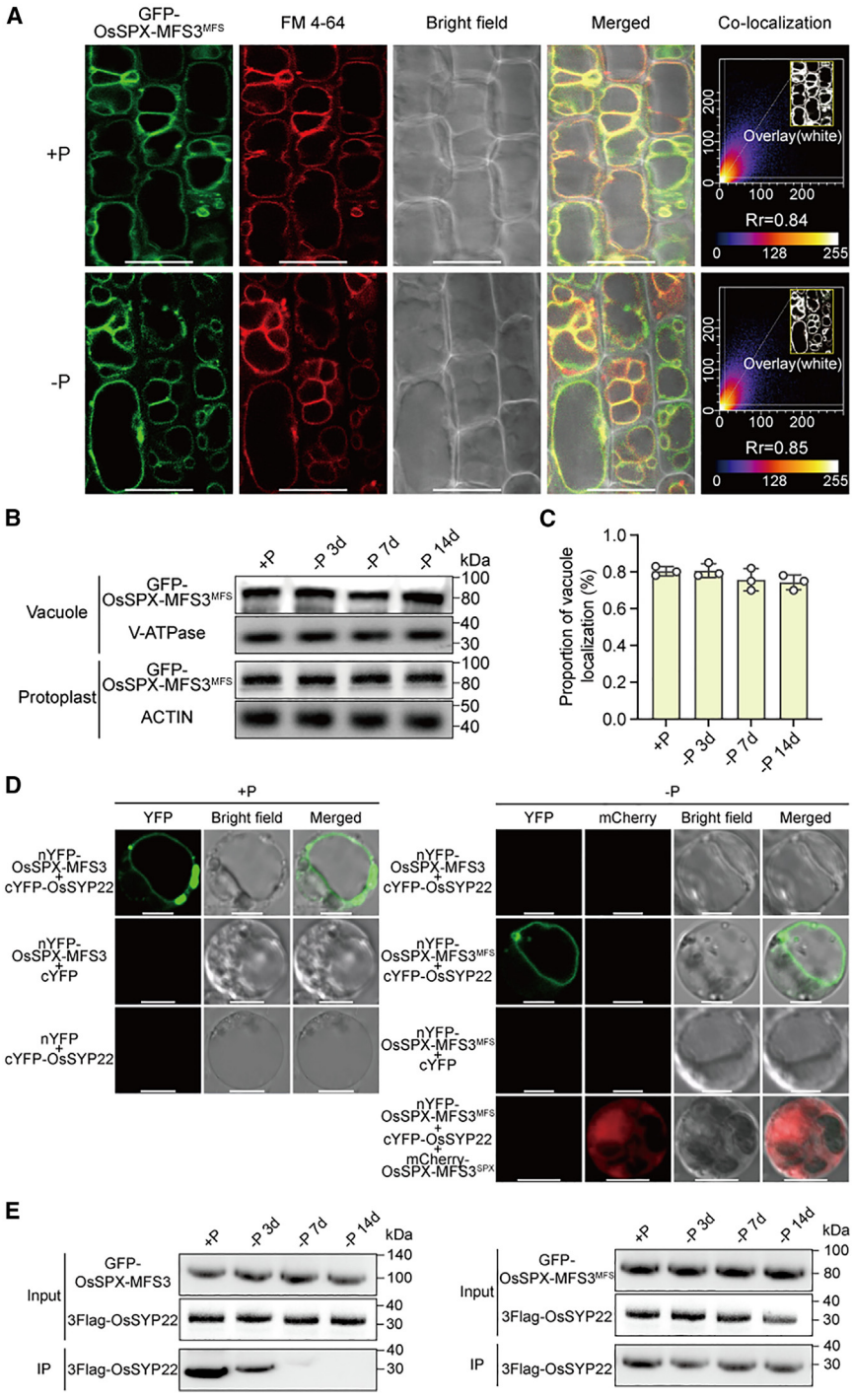

Figure 5. Function of the SPX domain of OsSPX-MFSs in their tonoplast localization.

(A) Confocal fluorescence imaging of a *GFP-OsSPX-MFS3^{MFS}* overexpression plant root. Roots of 7-day-old *GFP-OsSPX-MFS3^{MFS}* overexpression plants grown in Pi-replete or Pi-depleted conditions were sampled for fluorescence imaging. Tonoplasts were stained with the endocytotic tracer FM4-64 for 3 h. Scale bars, 20 μm. Co-localization analyses were performed with Coloc2 in ImageJ software. Rr represents the Pearson correlation coefficient.

(B and C) Effect of Pi supply on the distribution of GFP-OsSPX-MFS3^{MFS} in protoplasts and vacuoles. Two-week-old *GFP-OsSPX-MFS3^{MFS}* overexpression plants were transferred to Pi-depleted conditions for the number of days indicated. Protoplasts and tonoplasts were isolated separately, immunoblotted using GFP antibodies **(B)**, and quantified **(C)**. Rice β-actin and V-ATPase were detected as references for protoplast and vacuolar proteins, respectively. Quantification of GFP-OsSPX-MFS3^{MFS} relative to the reference protein was performed with Quantity Tools in Image Lab software. The proportions were calculated by comparing the level of GFP-OsSPX-MFS3^{MFS} protein in vacuoles to that in protoplasts.

(D) BiFC analysis of the interaction between OsSPX-MFS3 or OsSPX-MFS3^{MFS} and OsSYP22 under Pi-replete and Pi-depleted conditions. nYPF-OsSPX-MFS3 (or nYPF-OsSPX-MFS3^{MFS}) and cYFP-OsSYP22 were co-expressed in protoplasts isolated from NIP seedlings cultured in Pi-replete and Pi-depleted conditions. A construct with mCherry fused to the N terminus of the SPX domain (mCherry-OsSPX-MFS3^{SPX}) was used to determine the function of the SPX domain in the interaction between MFS and OsSYP22. Combinations of cYFP or nYFP with the corresponding nYFP-OsSPX-MFS3, nYFP-OsSPX-MFS3^{MFS}, and cYFP-OsSYP22 fusion constructs were used as negative controls. Scale bars, 20 μm.

(E) Co-IP assay of the interaction between OsSPX-MFS3 or OsSPX-MFS3^{MFS} and OsSYP22 in tobacco leaves grown in Pi-depleted conditions. *pro35S-GFP-OsSPX-MFS3* or *pro35S-GFP-OsSPX-MFS3^{MFS}* was co-expressed with *pro35S-3FLAG-OsSYP22* in tobacco leaves exposed to Pi-depleted conditions for the number of days indicated. Protein extracts were subjected to IP using anti-GFP magnetic beads and analyzed by immunoblotting with anti-FLAG and anti-GFP antibodies.

These results demonstrate that the SPX domain of OsSPX-MFS3 inhibits the interaction between the MFS domain and OsSYP22 under Pi-depleted conditions, thus disrupting the trafficking of OsSPX-MFS3 between the PVCs and the vacuole.

Function of the MFS domain of OsSPX-MFSs in mediating vacuolar Pi influx

To examine the functions of the SPX and MFS domains of OsSPX-MFS3 in plant Pi homeostasis, we generated plants overexpressing GFP-tagged OsSPX-MFS3^{SPX} and OsSPX-MFS3^{MFS} in the *osspx-mfs1/2/3* triple mutant background (Supplemental Figure 10). Selected overexpression lines, whose expression levels of *GFP-OsSPX-MFS3^{MFS}* or *GFP-OsSPX-MFS3^{SPX}* were similar to that of *OsSPX-MFS3* in NIP, were analyzed for phenotypes and Pi concentrations using NIP and *osspx-mfs1/2/3* plants as controls. Under Pi-replete conditions, growth of *OsSPX-MFS3^{MFS}/osspx-mfs1/2/3* plants was similar to that of NIP plants, whereas growth of *OsSPX-MFS3^{SPX}/osspx-mfs1/2/3* was similar to that of the *osspx-mfs1/2/3* triple mutant (Figure 6A). Expression of

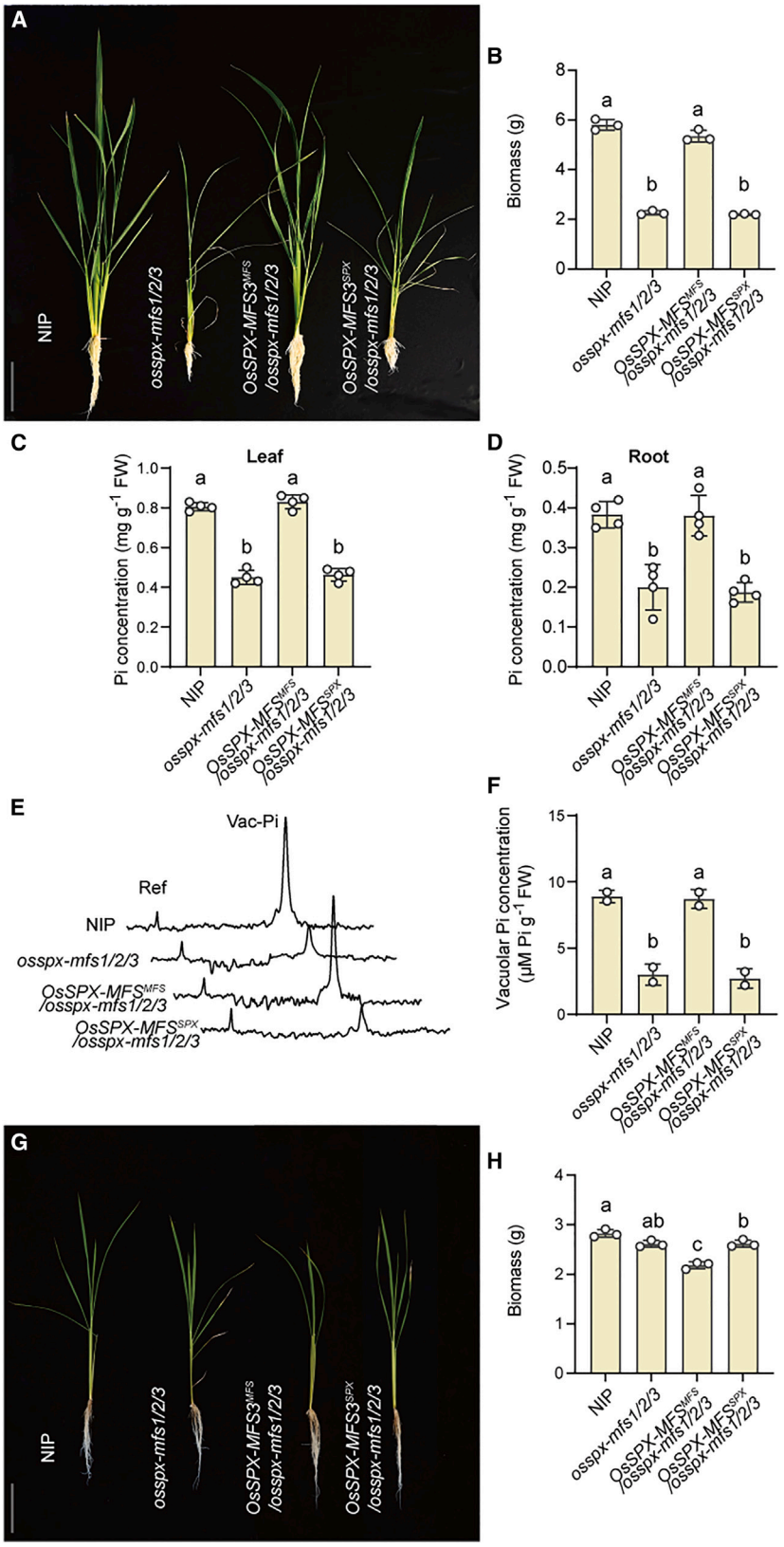

Figure 6. Function of the MFS domain of OsSPX-MFS3 in mediating vacuolar Pi influx.

(A–D) Phenotypic performance **(A)**, biomass **(B)**, and leaf **(C)** and root **(D)** Pi concentrations of 40-day-old NIP (wild-type), *osspx-mfs1/2/3*, *GFP-OsSPX-MFS3^{MFS}/osspx-mfs1/2/3*, and *GFP-OsSPX-MFS3^{SPX}/osspx-mfs1/2/3* plants under Pi-replete conditions. Scale bars, 10 cm.

(E) *In vivo* ^{31}P-NMR spectra from roots of the above rice plants grown under Pi-replete conditions and harvested at 2 weeks of age. Peaks from right to left are assigned to Vac-Pi and the reference (Ref; methylenediphosphonate) used to measure chemical shifts and for quantification.

(F) The calculated Vac-Pi concentrations of plants as in **(E)**.

(G and H) Phenotypic performance **(G)**, biomass **(H)** of 40-day-old NIP (wild-type), *osspx-mfs1/2/3*, *GFP-OsSPX-MFS3^{MFS}/osspx-mfs1/2/3*, and *GFP-OsSPX-MFS3^{SPX}/osspx-mfs1/2/3* plants under Pi-depleted conditions. Scale bars, 10 cm.

OsSPX-MFS3^{MFS}, but not *OsSPX-MFS3*^{SPX}, complemented the leaf and root growth defects of *osspx-mfs1/2/3* plants, reduced leaf and root growth (Figures 6A and 6B). In addition, expression of *OsSPX-MFS3*^{MFS} complemented the Pi decrease in the triple mutant (Figures 6C–6F). The Pi concentrations of leaves and roots in *OsSPX-MFS3*^{MFS}*/osspx-mfs1/2/3* plants were similar to those in NIP and higher than those in *OsSPX-MFS3*^{SPX}*/osspx-mfs1/2/3* and *osspx-mfs1/2/3* triple mutants (Figures 6C and 6D). The vacuolar Pi concentration of the *OsSPX-MFS3*^{MFS}*/osspx-mfs1/2/3* overexpression line was also higher than that of the *OsSPX-MFS3*^{SPX}*/osspx-mfs1/2/3* overexpression line and the *osspx-mfs1/2/3* triple mutant (Figures 6E and 6F). By contrast, under Pi-depleted conditions, the *OsSPX-MFS3*^{MFS}*/osspx-mfs1/2/3* had lower biomass than NIP and *OsSPX-MFS3*^{SPX}*/osspx-mfs1/2/3* (Figures 6G and 6H). These data indicate that the SPX and MFS domains in OsSPX-MFS3 have different functions. The MFS domain of OsSPX-MFS3 functions as a Pi transporter, as OsSPX-MFS3^{MFS} lines still had the capacity for vacuolar Pi sequestration. The SPX domain of *OsSPX-MFS3* plays an important role in plant adaptation to low Pi.

DISCUSSION

In this study, we found that tonoplast localization of OsSPX-MFS3 and the other two OsSPX-MFSs is significantly inhibited under Pi-depleted conditions, resulting in their retention in the PVCs (Figures 1 and 2). Understanding the mechanism of trafficking of rice SPX-MFSs is critical for improving plant Pi buffering through biotechnology. We dissected the function of the rice SPX-MFSs into two parts corresponding to their SPX domain and MFS domain, respectively. The SPX domain is exposed to the cytosol, sensing the intracellular Pi level and subsequently regulating the tonoplast localization of OsSPX-MFSs to buffer cellular Pi concentration (Figures 3C and 3D), whereas the MFS domain functions as a vacuolar Pi influx transporter (Figure 6).

We demonstrated that the SNARE proteins OsSYP21 and OsSYP22 interact with the MFS domain of OsSPX-MFS3 and facilitate trafficking of OsSPX-MFS3 from the PVCs to the tonoplast (Figures 3B, 3E, and 3F). The reason why the *ossyp21* mutant does not show altered tonoplast targeting of GFP-OsSPX-MFS3 (Figure 4) may be due to functional compensation by *OsSYP22* or to its relatively lower expression compared with *OsSYP22* (Supplemental Figure 2). Thus, although both OsSYP21 and OsSYP22 are involved in regulating plant Pi homeostasis by facilitating OsSPX-MFS trafficking and tonoplast localization, OsSYP22 appears to play the major role. Indeed, expression of the negative-dominant form of OsSYP22 led to retention of OsSPX-MFS3 in the PVCs. However, we could not exclude the possibility that the negative-dominant mutant of OsSPY22 may have had a negative effect on the function of OsSYP21. Thus, even though the OsSPX-MFS3 localization pattern did not change in the *ossyp21 mutants*, *in vivo* OsSPY21 may play some role.

There are two possible mechanisms by which the SPX domain inhibits interaction of the MFS domain with OsSYP22 under Pi-depleted conditions: (1) in the absence of InsPs under Pi-depleted conditions, the SPX domain may occupy the OsSYP22 binding site of the MFS domain, preventing its interaction with OsSYP22, or (2) other protein component(s) may associate with the SPX domain in the presence/absence of InsPs, which directly regulates the interaction between the MFS domain and OsSYP22. A number of studies have shown that SPX domains transmit Pi signals through protein–protein interactions (Dong et al., 2019; Lv et al., 2014; Puga et al., 2014; Ried et al., 2021; Wang et al., 2014; Wild et al., 2016; He et al., 2021; Hu et al., 2019).

To test these possibilities, we performed structure predictions of the free state of OsSPX-MFS3 and its complex with OsSYP22 using the latest version of AlphaFold2 (AF2). The AF2 predictions suggested that OsSPX-MFS3 could form two distinct conformations. In one conformation, the SPX domain departs from the MFS domain, resulting in an open pocket in the TM region of the MFS domain that might be used for Pi transport. In the other conformation, this potential Pi pocket is blocked by the region (L211 to E231, consisting of an alpha-helix and a loop) between SPX and MFS, which is likely in a self-inhibited state (Figure 7A). An electrostatics surface analysis of the SPX domain revealed a highly positively charged surface on its N-terminal regions including helices 1, 2 (K6–K31), and 4 (K112–R134), which might serve as the binding pocket for the negatively charged InsPs via electrostatic interactions (Figure 7B). BiFC experimental interaction data showed that the SPX domain interacts with the MFS domain under Pi-depleted conditions (Figure 7E). Co-IP data showed that in the presence of InsP6, the self-interaction between SPX and the MFS domain was abolished, indicating that InsP binding might induce a conformational change in SPX and promote the interactions between SPX and MFS (Figure 7F). Three amino acids in the SPX domain are defined as the phosphate-binding cluster (PBC) sites and are vital for efficient ligand binding (Wild et al., 2016). Sequence alignment indicated that Y23, K27, and K130 were the PBC sites in OsSPX-MFS3. OsSPX-MFS3^{PBS}, in which the three amino acids were mutated to Y23F, K27A, and K130A, showed a lower tonoplast localization pattern under Pi-replete conditions (Figure 7G). Taken together, these data suggest that the absence of bound InsPs in the SPX domain promotes interaction between the SPX and MFS domains, inhibiting the interaction between OsSPX-MFS3 and OsSYP22 and thus negatively affecting trafficking of OsSPX-MFS3 to the tonoplast.

The predicted structures of OsSPX-MFS3 in complex with OsSYP22 suggested that the C-terminal helix of OsSYP22 inserts into the membrane and binds with the first half of the MFS domain, which consists of TM helices 1–6 (Figures 7C and 7D). It also revealed that the SynN domain of OsSYP22 interacts with the SPX domain and the hydrophilic surface of the MFS domain at the same time, like a sandwich (Figure 7D). Our Y2H data showed that the t-SNARE domain of OsSYP21/22 alone could not interact with OsSPX-MFS3$^{SPX\text{-}2TM}$ or OsSPX-MFS3$^{SPX\text{-}6TM}$. It is possible that this interaction needs to be stabilized by other domains (SynN or TM helix) in OsSYP21/22 (Figure 3B). On the basis of these data, we propose that under Pi-depleted conditions, the Pi pocket in the MFS domain is blocked by the helix next to the SPX domain, resulting in self-inhibition of OsSPX-MFS3, and that the OsSYP21/22 binding site of the MFS domain is occupied by the SPX domain, thereby trapping the protein in the PVCs. By contrast, under Pi-replete conditions, binding of InsPs to the SPX domain induces a

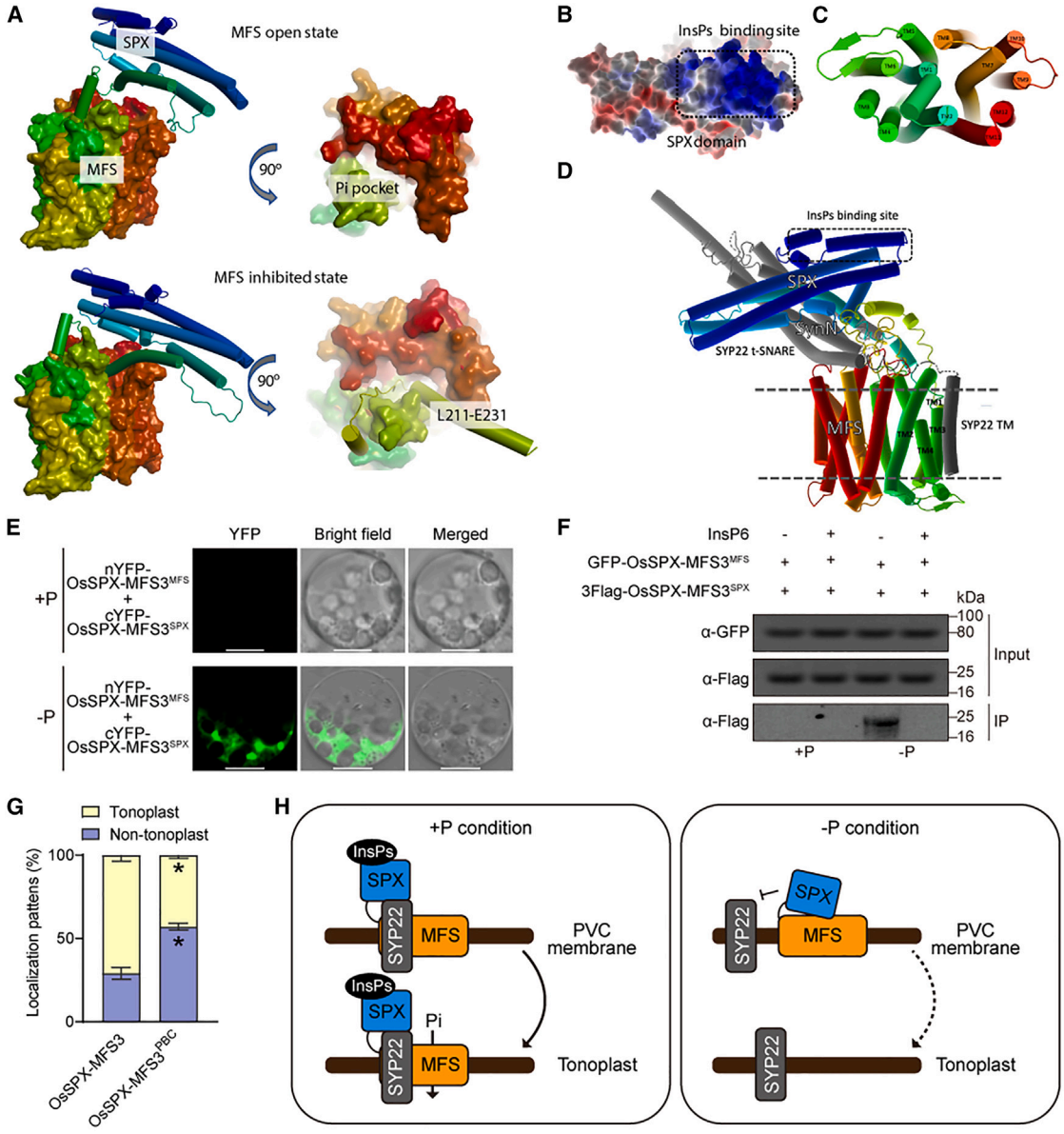

Figure 7. Potential mechanism by which the SPX domain senses intracellular Pi levels and regulates the trafficking of OsSPX-MFS3.

(A) Structures of OsSPX-MFS3 predicted by AlphaFold2. OsSPX-MFS3 was predicted to form two possible conformations, one with an open pocket in the transmembrane region that may be used for Pi transport (upper panel) and the other in an inhibited state in which the potential Pi pocket is blocked by the helix formed between SPX and the MFS domain ranging from L211 to E231 (lower panel).

(B) An electrostatics surface analysis of the SPX domain revealed a highly positively charged surface on its N-terminal region, including helices 1, 2 (K6–K31), and 4 (K112–R134), which may serve as the binding site for negatively charged InsPs.

(C) The predicted structure of MFS suggested that it contains 12 transmembrane helices.

(D) One of the predicted models of the complex suggested that the C-terminal region of OsSYP22 forms an α-helix that inserts into the membrane and binds to the N-terminal half of the MFS domain, consisting of TM helices 1–6.

(E) BiFC analysis of the interaction between nYFP-OsSPX-MFS3^{MFS} and cYFP-OsSPX-MFS3^{SPX} in Pi-replete and Pi-depleted conditions. Scale bars, 20 μm.

(F) Co-IP assay of GFP-OsSPX-MFS3^{MFS} with FLAG-OsSPX-MFS3^{SPX} in tobacco leaves cultured in Pi-replete and Pi-depleted conditions in the presence of InsP6.

(G) Quantification of GFP-OsSPX-MFS3 and GFP-OsSPX-MFS3^{PBC} localization patterns under Pi-replete conditions. PBC, phosphate binding cluster site.

(H) Potential mechanism by which the SPX domain senses intracellular Pi levels and regulates the trafficking of OsSPX-MFS3. Under Pi replete condition, OsSPX-MFS3 target to the tonoplast via interaction with OsSYP22.

Under Pi depleted condition, the interaction with OsSYP22 is abolished by self-interaction, resulting in the retention in the PVCs.

large-scale conformational adjustment of the SPX domain, resulting in exposure of the OsSYP22 binding site in the MFS domain. This allows the binding of OsSYP21/22 to OsSPX-MFS3, which further facilitates the trafficking of OsSPX-MFS3 to the tonoplast.

Binding of InsPs to SPX also induces the release of the regulatory helix from the Pi transport pocket in the MFS domain, allowing Pi transport. This is consistent with another model proposed in *Arabidopsis* (Luan et al., 2022). In the latter study, tonoplast-located SPX-MFS (AtVPT1) was proposed to have two conformations, one that allows transport of Pi, and one in which auto-inhibition of the SPX domain prevents transport under Pi-replete conditions. Thus, both models propose an auto-inhibitory role of the SPX domain. The findings presented here add further resolution and complexity to the post-translational control of OsSPX-MFS3. The two studies revealed different post-translational regulatory mechanisms because they differed in aims and experimental design. First, we performed studies with rice rather than *Arabidopsis*. Rice is a longer-lived plant and will thus require different regulatory mechanisms to deal with nutrient availability. Second, our kinetic analysis revealed that it took up to 7 days to observe inhibition of transport under Pi-depleted conditions in rice, longer than the 5-day time course used in the *Arabidopsis* study (Luan et al., 2022). The kinetics may differ between species. Moreover, we provided three distinct lines of evidence: protein trafficking localization using markers for various compartments in the endomembrane system, protein–protein interactions (Y2H, BiFC, and Co-IP), and strong genetic evidence obtained by genetic manipulation of *OsSYP22*. The two models are not contradictory and may in fact be synergistic. Under Pi-depleted conditions, a relatively fast mechanism for inhibiting or slowing down vacuolar Pi transport is to inhibit the transport protein that is already in the tonoplast membrane, providing a first response to limited Pi availability. If phosphate limitation continues, an additional mechanism is engaged to inhibit trafficking of the Pi transporter to the membrane. This means that a transient deficiency in Pi availability does not completely reduce the availability of vacuole-located OsSPX-MFS3, which would be undesirable, as Pi assimilation will need to resume when Pi becomes available again. However, longer term deficiency reduces the amount of tonoplast-located OsSPX-MFS3.

Although this study and its conclusions were based primarily on rice OsSPX-MFS3, interactions between SPX-MFSs and SYP2 proteins were also found for the other two rice SPX-MFSs and all three *Arabidopsis* SPX-MFSs (VPT1–3; Supplemental Figure 3), suggesting a conserved cellular mechanism for regulation of Pi homeostasis in response to changes in Pi availability. Loss of InsP binding was recently reported to decrease the ion transport activity of VPT1 (Luan et al., 2022). Under Pi-deficiency conditions, N-terminal α-helixes number 7 and 8 blocked the ion transport channel on the MFS domain (Luan et al., 2022). Our data differ from those reported (Luan et al., 2022) on the self-interaction of SPX and the MFS domain under Pi-replete conditions. However, both studies suggest that under Pi-depleted conditions, OsSPX-MFS3^{SPX} (corresponding to VPT1α1–8) inhibits the function of SPX-MFS proteins by interacting with the MFS domain. We noted that the two studies used different durations of low P treatment. In *Arabidopsis*, VPT1 showed inhibition of Pi transport activity and no change in localization after 4–5 days of Pi-depletion treatment (Luan et al., 2022). In our study, the shift in OsSPX-MFS3 localization occurs after 7–14 days of Pi-deficiency treatment. It seems that when the plant begins to experience Pi deficiency (short Pi-depletion time), the Pi transport activity of SPX-MFS already located on the tonoplast is inhibited. As Pi deficiency persists, newly synthesized SPX-MFS proteins are not trafficked to the tonoplast. Both mechanisms could work together to ensure the maintenance of stable cytoplasmic Pi concentrations.

In summary, this study reveals one mechanism by which plant SPX-MFSs respond to intracellular Pi concentration (Figure 7H), i.e., integrating Pi concentration signals and vacuolar Pi sequestration capacity through protein–protein interactions, and provides a new understanding of the regulatory mechanisms that underlie plant phosphate homeostasis.

METHODS

Plant materials and growth conditions

Wild-type rice (*Oryza sativa* L. *japonica*) cv. Nipponbare and the *osspx-mfs1/2/3* mutant were used for physiological experiments and rice transformation. Hydroponic experiments were performed using a modified culture solution (Yoshida et al., 1976) containing 1430 μM NH_4NO_3, 320 μM NaH_2PO_4, 510 μM K_2SO_4, 1000 μM $CaCl_2$, 1640 μM $MgSO_4$, 9 μM $MnCl_2$, 0.15 μM $CuSO_4$, 0.15 μM $ZnSO_4$, 0.08 μM $(NH_4)_6Mo_7O_{24}$, 0.02 μM H_3BO_3, 125 μM EDTA-Fe, and 250 mM $NaSiO_3$ (pH 5.5). Rice seeds were germinated in tap water with 1% nitric acid for 2 d and then transferred to hydroponic culture. Rice seedlings were grown in a growth room with day/night temperatures of 30°C/22°C and a 16-h photoperiod (200 mmol photons m^{-2} s^{-1}). We used 320 μM NaH_2PO_4 and 16 μM NaH_2PO_4 (1/20) for Pi-replete and Pi-depleted treatments, respectively.

Construction of vectors for transformation

For overexpression constructs, the full-length CDSs of *OsSYP21*, *OsSYP22*, and *OsSYP22-ND* (without the C-terminal TM helix; 245–267 aa) were inserted into modified pCAMBIA1300 (Wang et al., 2015) by seamless cloning. *GFP* was fused at the N terminus with target genes and driven by the *35S* promoter.

For complementation of the *osspx-mfs1/2/3* mutant, full-length *OsSPX-MFS3*, *OsSPX-MFS3^{SPX}*, and *OsSPX-MFS3^{MFS}* were inserted into modified pTF101 (Ying et al., 2017) by seamless cloning. *GFP* was fused at the N terminus with target genes and driven by the *35S* promoter. The resulting constructs, as well as *pC1300-GFP-OsSYP21* and *pC1300-GFP-OsSYP22* vectors, were used for transformation of NIP and the *osspx-mfs1/2/3* mutant.

Constructs were transformed into callus derived from mature seeds of NIP or the indicated mutant via *Agrobacterium tumefaciens* EHA105. The primers used for all amplifications are listed in Supplemental Table 3.

RNA isolation and qRT–PCR

Total RNA was extracted from plant samples using the RNA-easy Isolation Reagent (Vazyme) according to the manufacturer's recommendations. First-strand cDNAs were synthesized from total RNA using a PrimeScript RT reagent Kit with gDNA Eraser. Quantitative RT (qRT)–PCR was performed using TB Green qPCR Master Mix (Takara) on a LightCycler 480 thermocycler (Roche Diagnostics). Relative gene expression was calculated by the $2^{-\Delta\Delta Ct}$ method using the housekeeping gene *OsACT1* as an internal reference. Primers used for qRT–PCR are given in Supplemental Table 3. All experiments were performed with three biological and two technical replications.

Measurement of Pi concentration

Leaves and roots of rice seedlings from Pi-replete or Pi-deficient conditions were sampled separately. The Pi concentration was measured using a previously described procedure (Wang et al., 2009). In brief, fresh samples (50 μg) were homogenized with 50 μl of 5 M H_2SO_4 and 3 ml H_2O. The homogenate was transferred to 1.5-ml tubes and centrifuged at 10 000 × *g* for 10 min at 4°C. The supernatant was collected and diluted to an appropriate concentration. The diluted supernatant was mixed with malachite green reagent in a 3:1 ratio and analyzed after 30 min. The absorption values for the solution at 650 nm were determined using a Spectroquant NOVA 60 spectrophotometer (Merck, Darmstadt, Germany). The Pi concentration was calculated from a standard curve generated with various concentrations of KH_2PO_4.

Nuclear magnetic resonance spectroscopy

About 0.07 g (fresh weight) of roots from 2-week-old plants were packed into a 5-mm-diameter nuclear magnetic resonance (NMR) tube equipped with a perfusion system connected to a peristaltic pump. *In vivo* ^{31}P-NMR spectra of the roots were recorded on a Bruker Ascend 600 NMR spectrometer (Bruker, Rheinstetten, Germany) with MestReNova software version 6.1.1-6384. The ^{31}P-NMR spectra were recorded at a 242.9-MHz lock with deuteroxide in the capillary and water. The ^{31}P-NMR acquisition conditions were as follows: 30° pulse angle, 1500 scans, and a spectral window of 16 kHz. Chemical shifts were measured relative to the signal from a glass capillary containing 10 mM methylenediphosphonic acid as a reference, which is at 18.9 ppm relative to the signal from 85% H_3PO_4.

Isolation of protoplasts, vacuoles, and tonoplasts

Ten-day-old rice seedlings grown on culture medium supplemented with 320 μM Pi or 16 μM Pi were sampled for protoplast, vacuole, and tonoplast isolation.

Stems and leaves of 50 rice seedlings were cut into approximately 0.5-mm strips using a razor blade. The strips were placed into a Petri dish with 10 ml of enzyme solution (1.5% [w/v] cellulose and 0.3% [w/v] macerozyme in K3 medium). We applied a vacuum for 1 h for infiltration of the enzyme solution and incubated it for about 4 h in the dark with gentle shaking (approximately 40 rpm) at room temperature. The enzyme solution was removed, and 10 ml of W5 medium (154 mM NaCl, 125 mM $CaCl_2$, 5 mM KCl, and 2 mM MES, pH 5.7) was added with gentle shaking (approximately 80 rpm) for 1 h to release the protoplasts. The solution was filtered through 35-mm nylon mesh and centrifuged at 1500 rpm for 4 min to collect the protoplasts.

Rice vacuoles were isolated following previously published methods (Robert et al., 2007). A 2-ml aliquot of protoplast lysis buffer (200 mM sorbitol, 10% Ficoll-400, 20 mM EDTA, 10 mM HEPES-OH, 0.15% BSA, 2 mM DTT, 5 μg ml^{-1} neutral red, pH 8.0) was added to the previously extracted rice protoplasts, and the solution was incubated at 37°C for 2–10 min. The solution was inspected using a light microscope for protoplast disruption and vacuolar release. The solution was transferred into an ultra-clear centrifugation tube, then overlayed with 3 ml 4% Ficoll in vacuole buffer (500 mM sorbitol, 10 mM HEPES-OH, 0.15% BSA, 1 mM DTT, 2 μg ml^{-1} leupeptin, 2 μg ml^{-1} antipain). One milliliter of ice-cold vacuole buffer was gently added to the top phase. Vacuoles were isolated by ultracentrifugation (71 000 × *g*, 50 min, 4°C), after which intact vacuoles were visible as an interface between the top and middle phases.

For further tonoplast isolation (Zouhar, 2017), isolated vacuoles were centrifuged at 100 000 × *g* for 1 h at 4°C. The pellets were washed three times with PBS, then loaded onto an SDS–PAGE gel with 2× Laemmli buffer.

Subcellular localization and BiFC

For transient expression of constructs in rice protoplasts, the coding regions of *OsSPX-MFS3*, *OsSPX-MFS3^{MFS}*, and *OsSPX-MFS3^{SPX}* were amplified using attB-containing primers and cloned into pDEST-cGFP (Carrie et al., 2008). *OsSPX-MFS3^{MFS}* was amplified and cloned into pSAT4-mCherry-N1 (Lee and Gelvin, 2014) by seamless cloning. *OsSPX-MFS3*, *OsSPX-MFS3^{MFS}*, *OsSPX-MFS3^{SPX}*, *OsSYP21*, and *OsSYP22* were cloned into the BiFC vectors pSAT6-nEYFP-N1 and pSAT6-nEYFP-C1 by seamless cloning to generate *nYFP-OsSPX-MFS3*, *nYFP-OsSPX-MFS3^{MFS}*, *cYFP-OsSPX-MFS3^{SPX}*, *cYFP-OsSYP21*, and *cYFP-OsSYP22*. For transient expression of constructs in tobacco leaves, target genes were cloned into either C-terminal or N-terminal fragments of YFP vectors (Yang et al., 2007) by seamless cloning to generate *nYFP-OsSPX-MFS1*, *nYFP-OsSPX-MFS2*, *nYFP-OsSPX-MFS3*, *cYFP-OsSYP21*, and *cYFP-OsSYP22*. Primers are listed in Supplemental Table 3.

AtWAK2-mCherry, GmMAN1-mCherry, VHA-A1-mCherry, mCherry-AtARA7, and vac-rk/CD3-975 were used as ER, Golgi, TGN, PVC, and tonoplast markers, respectively (Nelson et al., 2007). For rice protoplast transformation, 10 mg plasmid DNA of each construct was transformed into 0.2 ml protoplast suspension and incubated at 30°C in the dark for 12–15 h. For transient expression in tobacco leaves, the constructs were delivered by *Agrobacterium*-mediated infiltration (*A. tumefaciens* EHA105) as described previously (Walter et al., 2004), and fluorescence was imaged three days after infiltration. Fluorescence signals were detected using an LSM 710 NLO confocal laser scanning microscope (Zeiss, Göttingen, Germany). Excitation/emission wavelengths were 488 nm/506–538 nm for YFP and GFP, 561 nm/575–630 nm for mCherry, and 405 nm/465–480 nm for cell wall and CFP.

For the FM4-64 staining time course, 7-day-old GFP-OsSPX-MFS3 overexpression seedlings cultured under low-Pi conditions were incubated in medium containing 5 mM FM4-64 for the indicated times.

FM4-64 staining of tonoplasts was performed according to a published protocol (Scheuring et al., 2015). In brief, one-week-old rice seedlings were incubated in a culture medium containing 5 mM FM4-64 for 30 min in the dark. The seedlings were then transferred to fresh medium without FM4-64 in the dark for an additional 3 h and imaged by confocal microscopy.

Wortmannin treatment was performed with rice hydroponic medium containing 33 μM wortmannin dissolved in dimethyl sulfoxide (DMSO) for 2 h.

Ratiometric fluorescence imaging

roGFP2 offers the largest dynamic range at the fixed excitation wavelengths (Brach et al., 2009). roGFP2 fluorescence was excited at 405 and 488 nm in multi-tracking mode with line switching. To improve the signal-to-noise ratio, all images were collected using a mean of 4. roGFP2 fluorescence was collected using a band-pass filter at 505–530 nm. To minimize the influence of noise on the final ratio image, only cells whose fluorescence excited at 405 nm was at least five times higher than the background were used for further analysis. Ratiometric analysis of non-saturated images was performed using ImageJ software. For the proteins destined for distal compartments in the secretion pathway, samples were incubated with 50 μM BFA for 8 h as an inhibitor of ER–Golgi transport.

Protein isolation and immunoblot analysis

For total protein extraction, plant tissues were ground in liquid nitrogen and dissolved in SDS extraction buffer containing 2% (w/v) SDS, 60 mM Tris–HCl (pH 8.5), 2.5% (v/v) glycerol, 0.13 mM EDTA, 1 mM phenylmethylsulfonyl fluoride, and a protease inhibitor cocktail (Sigma-Aldrich). Plant tissues were ground in liquid nitrogen, and membrane proteins were isolated using a Plant Fractionated Protein Extraction Kit (PE0240, Sigma-Aldrich) to isolate hydrophobic proteins. For each sample, 50 μg

of protein sample was subjected to electrophoresis in SDS–PAGE gels, transferred to polyvinylidene fluoride (PVDF) membranes, and analyzed by immunoblotting using anti-FLAG (1:5000, ABclonal), anti-HIS (1:5000, ABclonal), anti-GST (1:5000, ABclonal), anti-β-actin (1:5000, ABclonal), anti-GFP (1:2000, Thermo Fisher Scientific), and anti-V-ATPase (1:2000; Agrisera) antibodies. Bound antibodies were visualized with ECL substrate (Millipore) using the ChemDoc XRS system (Bio-Rad). Quantitative analysis of immunoblots was performed using Quantity Tools in Image Lab software (Bio-Rad).

Y2H assay

Y2H assays were performed using a split-ubiquitin system following the instructions provided with the DUALmembrane pairwise interaction kit (Dualsystems Biotech, Zurich, Switzerland). Full-length, SPX-2TM, SPX-6TM, and SPX domain versions of *OsSPX-MFS3*, SPX-2TM versions of *OsSPX-MFS1,2*, and *AtVPT1,2,3* were subcloned in frame into pBT3-STE to generate *pBT3-STE-Preys*. Full-length, TM-helix-free, SynN domain, and t-SNARE domain versions of *OsSYP21* and *OsSYP22* and full-length versions of *OsSYP21*, *OsSYP22*, *AtSYP21*, *AtSYP22*, and *AtSYP23* were cloned in frame into pPR3N to generate *pPR3N-Baits*. Sequence data of all truncated proteins are provided in Supplemental Table 2. The constructs were co-transformed into yeast strain NMY51 and plated onto medium without Trp and Leu to select positive clones. Protein–protein interactions were indicated by the growth of yeast colonies on medium lacking Leu, Trp, His, and Ade. The bait APP-Cub expressing the type I integral membrane protein APP (amyloid A4 precursor protein) was used as a control that could interact with NubI but not with NubG.

Co-IP assay

Co-expression of GFP-OsSPX-MFS3 (or GFP-OsSPX-MFS3^{SPX} or GFP-OsSPX-MFS3^{MFS}) with 3FLAG-OsSYP21 (or 3FLAG-OsSYP22) was performed in tobacco leaves cultured in hydroponic medium with and without Pi supply. GFP and FLAG empty vectors were used as negative controls. Co-IP assays were preformed using a GFP-Trap Agarose Kit (Chromotek, Planegg-Martinsried, Germany) according to the manufacturer's instructions. GFP-tagged proteins and FLAG-tagged proteins were detected using anti-GFP (Themo Fisher Scientific) and anti-FLAG (ABclonal) antibodies, respectively. For InsP6 treatment, the corresponding constructs were co-transformed into tobacco leaves with 20 μM of InsP6 (P8810; Sigma-Aldrich), and samples were harvested after 2 days for assays.

Structure prediction

The structures of the free state of OsSPX-MFS3 and its complex with SYP22 were predicted using AlphaFold (version 2.2.0; Jumper et al., 2021) using the "monomer" deep learning models and its updated version AF2Complex (Gao et al., 2022), respectively, as implemented on our local computer cluster. Five structures were predicted for OsSPX-MFS3 and also for its complex. The structures were visualized by PyMOL (PyMOL molecular Graphics System, version 2.5.2, Schrödinger). The electrostatics surface analysis was performed using the APBS Electrostatics plugin in PyMol.

Accession numbers

Sequence data from this article can be found in the Rice Genome Annotation Project (RGAP) database under the following accession numbers: OsSPX-MFS1 (LOC_Os04g48390); OsSPX-MFS2 (LOC_Os02g45520); OsSPX-MFS3 (LOC_Os06g03860); OsSYP21 (LOC_Os02g47440); OsSYP22 (LOC_Os01g15110); AtVPT1 (AT1G63010); AtVPT2 (AT4G11810); AtVPT3 (AT4G22990); AtSYP21 (AT5G16830); AtSYP22 (AT5G46860); AtSYP23 (AT4G17730); AtWAK2 (At1g21270); GmMAN1 (NM_001251128.1); VHA-A1 (AT2G28520); AtARA7 (AT4G19640).

SUPPLEMENTAL INFORMATION

Supplemental information is available at *Molecular Plant Online*.

FUNDING

This work was supported by the Ministry of Science and Technology of China (2021YFF1000400, 2021YFF1001204) and the National Natural Science Foundation of China (317723817qw4 111 Project (B14027).

AUTHOR CONTRIBUTIONS

R.G., Y.Y., and H.S. conceived the project. R.G., Y.Y., W.L., and Q.Z. carried out the design of transformation constructs and physiological characterization of mutants and transgenic plants. Y.W. carried out the structure prediction. R.G., C.M., J.W., and H.S. interpreted results and drafted the publication. All authors reviewed the manuscript.

ACKNOWLEDGMENTS

The authors would like to thank Shelong Zhang, Jiming Xu, and Yu Liu for technical assistance and Zhenyu Qi and Rui Sun from the Agricultural Experiment Station (AES) of Zhejiang University for plant propagation and field testing. Yong, Wang acknowledges the computational support from Xiaogan 3D Scientific Computing Center. No conflict of interest is declared.

Received: April 1, 2023
Revised: June 26, 2023
Accepted: July 13, 2023
Published: July 17, 2023

REFERENCES

Brach, T., Soyk, S., Muller, C., Hinz, G., Hell, R., Brandizzi, F., and Meyer, A.J. (2009). Non-invasive topology analysis of membrane proteins in the secretory pathway. Plant J. **57**:534–541.

Bucher, M., and Fabianska, I. (2016). Long-sought vacuolar phosphate transporters identified. Trends Plant Sci. **21**:463–466.

Carrie, C., Murcha, M.W., Kuehn, K., Duncan, O., Barthet, M., Smith, P.M., Eubel, H., Meyer, E., Day, D.A., Millar, A.H., and Whelan, J. (2008). Type II NAD(P)H dehydrogenases are targeted to mitochondria and chloroplasts or peroxisomes in Arabidopsis thaliana. FEBS Lett. **582**:3073–3079.

Chiou, T.J., and Lin, S.I. (2011). Signaling network in sensing phosphate availability in plants. Annu. Rev. Plant Biol. **62**:185–206.

Colombo, M., Raposo, G., and Théry, C. (2014). Biogenesis, secretion, and intercellular Interactions of exosomes and other extracellular vesicles. Annu. Rev. Cell Dev. Biol. **30**:255–289.

Di Sansebastiano, G.P., Barozzi, F., Piro, G., Denecke, J., and de Marcos Lousa, C. (2017). Trafficking routes to the plant vacuole: connecting alternative and classical pathways. J. Exp. Bot. **69**:79–90.

Dong, J., Ma, G., Sui, L., Wei, M., Satheesh, V., Zhang, R., Ge, S., Li, J., Zhang, T.E., Wittwer, C., et al. (2019). Inositol Pyrophosphate InsP(8) Acts as an Intracellular Phosphate Signal in Arabidopsis. Mol. Plant **12**:1463–1473.

Ebine, K., Okatani, Y., Uemura, T., Goh, T., Shoda, K., Niihama, M., Morita, M.T., Spitzer, C., Otegui, M.S., Nakano, A., and Ueda, T. (2008). A SNARE complex unique to seed plants is required for protein storage vacuole biogenesis and seed development of Arabidopsis thaliana. Plant Cell **20**:3006–3021.

Foresti, O., daSilva, L.L.P., and Denecke, J. (2006). Overexpression of the Arabidopsis syntaxin PEP12/SYP21 inhibits transport from the prevacuolar compartment to the lytic vacuole in vivo. Plant Cell **18**:2275–2293.

Gao, M., An, D.N., Parks, J.M., and Skolnick, J. (2022). AF2Complex predicts direct physical interactions in multimeric proteins with deep learning. Nat. Commun. **13**:1.

Guan, Z., Zhang, Q., Zhang, Z., Zuo, J., Chen, J., Liu, R., Savarin, J., Broger, L., Cheng, P., Wang, Q., et al. (2022). Mechanistic insights

into the regulation of plant phosphate homeostasis by the rice SPX2 - PHR2 complex. Nat. Commun. **13**:1581.

Guo, R., Zhang, Q., Ying, Y., Liao, W., Liu, Y., Whelan, J., Chuanzao, M., and Shou, H. (2023). Functional characterization of the three Oryza sativa SPX-MFS proteins in maintaining phosphate homoeostasis. Plant Cell Environ. **46**:1264–1277.

Gutiérrez-Alanís, D., Ojeda-Rivera, J.O., Yong-Villalobos, L., Cárdenas-Torres, L., and Herrera-Estrella, L. (2018). Adaptation to phosphate scarcity: tips from Arabidopsis roots. Trends Plant Sci. **23**:721–730.

He, Q., Lu, H., Guo, H., Wang, Y., Zhao, P., Li, Y., Wang, F., Xu, J., Mo, X., and Mao, C. (2021). OsbHLH6 interacts with OsSPX4 and regulates the phosphate starvation response in rice. Plant J. **105**:649–667.

Hu, B., Jiang, Z., Wang, W., Qiu, Y., Zhang, Z., Liu, Y., Li, A., Gao, X., Liu, L., Qian, Y., et al. (2019). Nitrate-NRT1.1B-SPX4 cascade integrates nitrogen and phosphorus signalling networks in plants. Nat. Plants **5**:401–413.

Jahn, R., Lang, T., and Südhof, T.C. (2003). Membrane fusion. Cell **112**:519–533.

Jahn, R., and Scheller, R.H. (2006). SNAREs–engines for membrane fusion. Nat Rev Mol Cell Biol **7**:631–643. https://doi.org/10.1038/nrm2002.

Jumper, J., Evans, R., Pritzel, A., Green, T., Figurnov, M., Ronneberger, O., Tunyasuvunakool, K., Bates, R., Žídek, A., Potapenko, A., et al. (2021). Highly accurate protein structure prediction with AlphaFold. Nature **596**:583–589.

Jung, J.Y., Ried, M.K., Hothorn, M., and Poirier, Y. (2018). Control of plant phosphate homeostasis by inositol pyrophosphates and the SPX domain. Curr. Opin. Biotechnol. **49**:156–162.

Lambers, H. (2022). Phosphorus acquisition and utilization in plants. Annu. Rev. Plant Biol. **73**:17–42.

Lee, L.-Y., and Gelvin, S.B. (2014). Bimolecular fluorescence complementation for Imaging protein interactions in plant hosts of microbial pathogens. In Host-Bacteria Interactions: Methods and Protocols, pp. 185–208.

Liu, J., Yang, L., Luan, M., Wang, Y., Zhang, C., Zhang, B., Shi, J., Zhao, F.G., Lan, W., and Luan, S. (2015). A vacuolar phosphate transporter essential for phosphate homeostasis in Arabidopsis. Proc. Natl. Acad. Sci. USA **112**:E6571–E6578.

Liu, T.Y., Huang, T.K., Yang, S.Y., Hong, Y.T., Huang, S.M., Wang, F.N., Chiang, S.F., Tsai, S.Y., Lu, W.C., and Chiou, T.J. (2016). Identification of plant vacuolar transporters mediating phosphate storage. Nat. Commun. **7**:11095.

Lonetti, A., Szijgyarto, Z., Bosch, D., Loss, O., Azevedo, C., and Saiardi, A. (2011). Identification of an evolutionarily conserved family of inorganic polyphosphate endopolyphosphatases. J. Biol. Chem. **286**:31966–31974.

Luan, M., Zhao, F., Han, X., Sun, G., Yang, Y., Liu, J., Shi, J., Fu, A., Lan, W., and Luan, S. (2019). Vacuolar phosphate transporters contribute to systemic phosphate homeostasis vital for reproductive development in Arabidopsis. Plant Physiol. **179**:640–655.

Luan, M., Zhao, F., Sun, G., Xu, M., Fu, A., Lan, W., and Luan, S. (2022). A SPX domain vacuolar transporter links phosphate sensing and homeostasis in Arabidopsis. Mol. Plant **15**:1590–1601.

Lv, Q., Zhong, Y., Wang, Y., Wang, Z., Zhang, L., Shi, J., Wu, Z., Liu, Y., Mao, C., Yi, K., and Wu, P. (2014). SPX4 negatively regulates phosphate signaling and homeostasis through its interaction with PHR2 in Rice. Plant Cell **26**:1586–1597.

Nelson, B.K., Cai, X., and Nebenführ, A. (2007). A multicolored set of in vivo organelle markers for co-localization studies in Arabidopsis and other plants. Plant J. **51**:1126–1136.

Puga, M.I., Mateos, I., Charukesi, R., Wang, Z., Franco-Zorrilla, J.M., de Lorenzo, L., Irigoyen, M.L., Masiero, S., Bustos, R., Rodríguez, J., et al. (2014). SPX1 is a phosphate-dependent inhibitor of Phosphate Starvation Response 1 in Arabidopsis. Proc. Natl. Acad. Sci. USA **111**:14947–14952.

Ried, M.K., Wild, R., Zhu, J., Pipercevic, J., Sturm, K., Broger, L., Harmel, R.K., Abriata, L.A., Hothorn, L.A., Fiedler, D., et al. (2021). Inositol pyrophosphates promote the interaction of SPX domains with the coiled-coil motif of PHR transcription factors to regulate plant phosphate homeostasis. Nat. Commun. **12**:384.

Robert, S., Zouhar, J., Carter, C., and Raikhel, N. (2007). Isolation of intact vacuoles from Arabidopsis rosette leaf-derived protoplasts. Nat. Protoc. **2**:259–262.

Robinson, D.G., Langhans, M., Saint-Jore-Dupas, C., and Hawes, C. (2008). BFA effects are tissue and not just plant specific. Trends Plant Sci. **13**:405–408.

Rojas-Pierce, M. (2013). Targeting of tonoplast proteins to the vacuole. Plant Sci. **211**:132–136.

Sanderfoot, A.A., Assaad, F.F., and Raikhel, N.V. (2000). The Arabidopsis genome. An abundance of soluble N-ethylmaleimide-sensitive factor adaptor protein receptors. Plant Physiol. **124**:1558–1569.

Sanderfoot, A.A., Kovaleva, V., Bassham, D.C., and Raikhel, N.V. (2001). Interactions between syntaxins identify at least five SNARE complexes within the Golgi/prevacuolar system of the Arabidopsis cell. Mol. Biol. Cell **12**:3733–3743.

Scheuring, D., Schöller, M., Kleine-Vehn, J., and Löfke, C. (2015). Vacuolar staining methods in plant cells. Methods Mol. Biol. **1242**:83–92.

Secco, D., Wang, C., Shou, H., and Whelan, J. (2012a). Phosphate homeostasis in the yeast Saccharomyces cerevisiae, the key role of the SPX domain-containing proteins. FEBS Lett. **586**:289–295.

Secco, D., Jabnoune, M., Walker, H., Shou, H., Wu, P., Poirier, Y., and Whelan, J. (2013). Spatio-temporal transcript profiling of rice roots and shoots in response to phosphate starvation and recovery. Plant Cell **25**:4285–4304.

Secco, D., Wang, C., Arpat, B.A., Wang, Z., Poirier, Y., Tyerman, S.D., Wu, P., Shou, H., and Whelan, J. (2012b). The emerging importance of the SPX domain-containing proteins in phosphate homeostasis. New Phytol. **193**:842–851.

Shirakawa, M., Ueda, H., Shimada, T., Koumoto, Y., Shimada, T.L., Kondo, M., Takahashi, T., Okuyama, Y., Nishimura, M., and Hara-Nishimura, I. (2010). Arabidopsis Qa-SNARE SYP2 proteins localized to different subcellular regions function redundantly in vacuolar protein sorting and plant development. Plant J. **64**:924–935.

Smith, S.E., and Barker, S.J. (2002). Plant phosphate transporter genes help harness the nutritional benefits of arbuscular mycorrhizal symbiosis. Trends Plant Sci. **7**:189–190.

Südhof, T.C., and Rothman, J.E. (2009). Membrane fusion: grappling with SNARE and SM proteins. Science **323**:474–477.

Uemura, T., Ueda, T., Ohniwa, R.L., Nakano, A., Takeyasu, K., and Sato, M.H. (2004). Systematic analysis of SNARE molecules in Arabidopsis: dissection of the post-Golgi network in plant cells. Cell Struct. Funct. **29**:49–65.

Uemura, T., Morita, M.T., Ebine, K., Okatani, Y., Yano, D., Saito, C., Ueda, T., and Nakano, A. (2010). Vacuolar/pre-vacuolar compartment Qa-SNAREs VAM3/SYP22 and PEP12/SYP21 have interchangeable functions in Arabidopsis. Plant J. **64**:864–873.

Walter, M., Chaban, C., Schütze, K., Batistic, O., Weckermann, K., Näke, C., Blazevic, D., Grefen, C., Schumacher, K., Oecking, C., et al. (2004). Visualization of protein interactions in living plant cells

using bimolecular fluorescence complementation. Plant J. **40**:428–438.

Wang, C., Ying, S., Huang, H., Li, K., Wu, P., and Shou, H. (2009). Involvement of OsSPX1 in phosphate homeostasis in rice. Plant J. **57**:895–904.

Wang, C., Huang, W., Ying, Y., Li, S., Secco, D., Tyerman, S., Whelan, J., and Shou, H. (2012). Functional characterization of the rice SPX-MFS family reveals a key role of OsSPX-MFS1 in controlling phosphate homeostasis in leaves. New Phytol. **196**:139–148.

Wang, C., Yue, W., Ying, Y., Wang, S., Secco, D., Liu, Y., Whelan, J., Tyerman, S.D., and Shou, H. (2015). Rice SPX-Major Facility Superfamily3, a vacuolar phosphate efflux transporter, is involved in maintaining phosphate homeostasis in Rice. Plant Physiol. **169**:2822–2831.

Wang, Z., Ruan, W., Shi, J., Zhang, L., Xiang, D., Yang, C., Li, C., Wu, Z., Liu, Y., Yu, Y., et al. (2014). Rice SPX1 and SPX2 inhibit phosphate starvation responses through interacting with PHR2 in a phosphate-dependent manner. Proc. Natl. Acad. Sci. USA **111**:14953–14958.

Wickner, W. (2010). Membrane fusion: five Lipids, four SNAREs, three chaperones, two nucleotides, and a Rab, all dancing in a ring on yeast vacuoles. Annu Rev Cell Dev Bi **26**:115–136.

Wild, R., Gerasimaite, R., Jung, J.Y., Truffault, V., Pavlovic, I., Schmidt, A., Saiardi, A., Jessen, H.J., Poirier, Y., Hothorn, M., and Mayer, A. (2016). Control of eukaryotic phosphate homeostasis by inositol polyphosphate sensor domains. Science **352**:986–990.

Yang, X., Baliji, S., Buchmann, R.C., Wang, H., Lindbo, J.A., Sunter, G., and Bisaro, D.M. (2007). Functional modulation of the geminivirus AL2 transcription factor and silencing suppressor by self-interaction. J. Virol. **81**:11972–11981.

Yano, D., Sato, M., Saito, C., Sato, M.H., Morita, M.T., and Tasaka, M. (2003). A SNARE complex containing SGR3/AtVAM3 and ZIG/VTI11 in gravity-sensing cells is important for Arabidopsis shoot gravitropism. Proc. Natl. Acad. Sci. USA **100**:8589–8594.

Ying, Y., Yue, W., Wang, S., Li, S., Wang, M., Zhao, Y., Wang, C., Mao, C., Whelan, J., and Shou, H. (2017). Two h-type thioredoxins Interact with the E2 Ubiquitin conjugase PHO2 to fine-tune phosphate homeostasis in Rice. Plant Physiol. **173**:812–824.

Zhou, J., Hu, Q., Xiao, X., Yao, D., Ge, S., Ye, J., Li, H., Cai, R., Liu, R., Meng, F., et al. (2021). Mechanism of phosphate sensing and signaling revealed by rice SPX1-PHR2 complex structure. Nat. Commun. **12**:7040.

Zhu, J., Lau, K., Puschmann, R., Harmel, R.K., Zhang, Y., Pries, V., Gaugler, P., Broger, L., Dutta, A.K., Jessen, H.J., et al. (2019a). Two bifunctional inositol pyrophosphate kinases/phosphatases control plant phosphate homeostasis. Elife **8**:e43582.

Zhu, X.F., Liu, Y., Gai, X.T., Zhou, Y., Xia, Z.Y., Chen, L.J., Duan, Y.X., and Xuan, Y.H. (2019b). SNARE proteins SYP22 and VAMP727 negatively regulate plant defense. Plant Signal. Behav. **14**:1610300.

Zouhar, J. (2017). Isolation of vacuoles and the tonoplast. Methods Mol. Biol. **1511**:113–118.